

Influence of *décollement*-cover thickness variations in fold-and-thrust belts: Insights from centrifuge analog modeling

Pablo Santolaria^{a,*}, Lyal B. Harris^b, Antonio M. Casas^c, Ruth Soto^d

^a Institut de Recerca Geomodels, Departament de Dinàmica de la Terra i de l'Oceà, Universitat de Barcelona, Martí i Franquès s/n 08028, Barcelona, Spain

^b Institut National de la Recherche Scientifique, Centre Eau Terre Environnement, 490 rue de la Couronne, Québec, QC, G1K 9A9, Canada

^c Geotransfer (IUCA), Departamento de Ciencias de la Tierra, Universidad de Zaragoza, Pedro Cerbuna 12, 50009, Zaragoza, Spain

^d CN Instituto Geológico y Minero de España (CSIC), Unidad de Zaragoza, Zaragoza, Spain

ARTICLE INFO

Keywords:

Centrifuge analog modeling

Salt *décollement*

Salt inflation

Vertical axis rotation

Thrust salient

ABSTRACT

Centrifuge analog modeling incorporating thickness variations of *décollement* and overlying sedimentary cover is used to study thrust-wedge evolution on salt-detached contractional systems involving tapered sedimentary cover. From simpler, layer-cake to 3D tapered *décollement*-cover sequences, our models constrain wedge evolution: a more advanced front, where the cover is thicker, promotes differential frontal translation and triggers vertical axis rotation of several hinterland anticlines which appear towards the thinner cover area. In all cases, the *décollement* level is strongly sheared and tends to migrate laterally toward the thinner cover areas. Models are compared with previous analog models under normal gravity and the natural example of the South Pyrenean Central salient. All in all, we conclude that a 3D tapered *décollement*-cover basin architecture, as a sole factor, can determine the formation of a thrust salient formed by increasing structural curvature (progressive arc).

1. Introduction

Analog (physical) and numerical models based on field and geophysical data have provided essential information about the geometry, kinematics and dynamics of fold-and-thrust belts containing a weak, basal ductile *décollement* (e.g., Davis and Engelder, 1987; Koyi, 1998; Cotton and Koyi, 2000; Costa and Vendeville, 2002; Roca et al., 2006; Stockmal et al., 2007; Storti et al., 2007; Graveleau et al., 2012 and references therein; Ruh et al., 2012; Granado et al., 2021). Centrifuge analog modeling has historically been used to simulate salt detached fold-and-thrust belt systems using few cm-wide squeeze boxes (e.g., Koyi, 1988; Mulugeta, 1988; Liu and Dixon, 1990; Dixon and Tirrul, 1991; Dixon and Liu, 1992; Waffle et al., 2016) or large centrifuges hosting tens of cm-wide models (Noble and Dixon, 2011). More recently, Milazzo and co-authors (2021) compared centrifuge and analog models where thrust wedges formed over frictional to low-frictional basal detachments. The main features of thrust wedges underlain by a low-strength basal weak layer are (e.g., Davis and Engelder, 1987; Cotton and Koyi, 2000; Costa and Vendeville, 2002; Bahroudi and Koyi, 2003; Luján et al., 2003): (i) lower critical tapers, (ii) opposite fold and thrust vergence, and (iii) rapid localization of the deformation front along the outer *décollement* pinch-out. Most analog models analyzing the

effect of such *décollements* on thrust wedges have been conducted under a normal gravity field due to simpler setups and wider range of choice when considering dimensions and geometries (e.g., Costa and Vendeville, 2002; Graveleau et al., 2012 and references therein). These settings, however, show limitations, especially regarding the rheology and mechanical behavior of both the *décollement* (silicone polymers) and the cover (loose sand) levels. In particular, the brittle behavior of the latter prevents studying some particular effects such as the occurrence of buckle folds in the hanging wall of thrusts and their influence in the amount of total shortening along strike. In order to broaden the range of experimental materials (and behaviors) able to simulate sedimentary rocks, in this work we conduct experiments under higher vertical gravity by means of a centrifuge device, a technique used since the pioneering works of Ramberg in the sixties (Ramberg, 1963; 1967a,b) and developed thereafter (e.g., Koyi, 1988; Mulugeta, 1988; Liu and Dixon, 1990; Dixon and Spratt, 2004; Godin et al., 2011; Noble and Dixon, 2011).

Previous works studying experimental thrust wedges overlying a low-strength *décollement* have investigated a wide range of parameters playing a major role in their structural style. These parameters can be classified into the following groups. (1) Along- and/or across-strike changes on the properties of the basal *décollement*, mainly due to the presence of lateral and/or frontal pinch-outs of the viscous layer (e.g.,

* Corresponding author.

E-mail addresses: p.santolaria.otin@ub.edu (P. Santolaria), lyal.harris@inrs.ca (L.B. Harris), acasas@unizar.es (A.M. Casas), r.soto@igme.es (R. Soto).

<https://doi.org/10.1016/j.jsg.2022.104704>

Received 1 March 2022; Received in revised form 3 August 2022; Accepted 12 August 2022

Available online 18 August 2022

0191-8141/© 2022 The Authors. Published by Elsevier Ltd. This is an open access article under the CC BY-NC-ND license (<http://creativecommons.org/licenses/by-nc-nd/4.0/>).

Calassou et al., 1993; Cotton and Koyi, 2000; Schreurs et al., 2001; Turrini et al., 2001; Bahroudi and Koyi, 2003; Luján et al., 2003; Vidal-Royo et al., 2009; Milazzo et al., 2021). (2) Convergence velocity, because of the dependence of the effective viscosity of the *décollement* on the strain rate (e.g., Davis et al., 1983; Liu and Dixon, 1990; Weijermars et al., 1993; ten Grotenhuis et al., 2002; Luján et al., 2006). (3) The convergence direction, whose perpendicularity or obliquity to the backstop results in different structural patterns (e.g., Lickorish et al., 2002; Soto et al., 2006; Crespo-Blanc, 2008). (4) Presence of an only or several interbedded viscous layers and/or stratigraphic thickness variations (e.g., Letouzey et al., 1995; Corrado et al., 1998; Couzens-Schultz et al., 2003; Massoli et al., 2006; Storti et al., 2007; Santolaria et al., 2015; Borderie et al., 2018). (5) Syntectonic sedimentation and/or erosion (e.g., Smit et al., 2010; Darnault et al., 2016; Pla et al., 2019). (6) Interaction of two indenters acting successively or simultaneously (e.g., Munteanu et al., 2014; Soto et al., 2020). (7) the mechanical stratigraphy overlaying the basal *décollement* (e.g., Liu and Dixon, 1990; Dixon and Tirrul, 1991; Noble and Dixon, 2011; Waffle et al., 2016). In this work, we investigate the role played by different pre-contractual thickness changes (i.e., forelandward, lateral and forelandward-oblique cover thinning) on the structural architecture of salt-detached fold-and-thrust belts. In order to isolate variables, and to define the ductile flow pattern without lateral anisotropies, thickness changes imposed on the geometry of the *décollement* were gradual and there were not lateral pinch-outs. Using a well-established centrifuge modelling protocol (see Yakymchuk et al., 2012), our experimental program represents an innovative approach, in terms of set-up geometries and modelling materials to give clues for interpreting compressional salt tectonics in environments with varying sedimentary cover thickness to salt *décollement* thickness ratios. A “4D” view of the development of structures was achieved by visualizing the interior of the analog models using computed tomodensitometry (CT scanning, e.g., Ramberg, 1981; Dixon and Summers, 1985; Yakymchuk et al., 2012). Modeling results are discussed and compared to the South Central Pyrenean salient.

2. Methodology: centrifuge analog modeling

2.1. Rationale

The presence of a tapered low-strength *décollement* at the base of a pre-orogenic, also tapered sedimentary cover sequence determines the geometry, kinematics and structural style of fold-and-thrust belts (e.g., Storti et al., 2007). Both factors (i.e., low-strength *décollement* and pre-tectonic thickness variations) are very common in nature, and usually occur simultaneously, conditioned by the paleogeography of sedimentary basins. Nevertheless, they have been analyzed separately in most cases (e.g., Liu et al., 1992; Macedo and Marshak, 1999; Cotton and Koyi, 2000; Costa and Vendeville, 2002; Soto et al., 2002).

Previous centrifuge analog models aimed testing different parameters such as the influence of pre-existing salt bodies (Koyi, 1988), the basal friction (Mulugeta, 1988; Milazzo et al., 2021) or the mechanical stratigraphy (Liu and Dixon, 1990; Dixon and Tirrul, 1991; Dixon and Liu, 1992; Noble and Dixon, 2011; Yakymchuk et al., 2012; Waffle et al., 2016) but, as a common feature, they considered a layer-cake mechanical stratigraphy. Our experimental program is designed to study the influence of pre-orogenic thickness variations on the structural architecture and ductile flow patterns of thrust wedges. These variations can involve both the basal *décollement* and the sedimentary cover and different 2D patterns, such as forelandward-thinning, lateral-thinning and forelandward-oblique-thinning, or tridimensional variations. The advantage of centrifuge analog models resides in its versatility to use different low-density and viscous materials in order to replicate ductile deformation or folding at different levels within the crust (e.g., Dixon and Summers 1985; Dixon and Tirrul 1991; Hill et al., 2010; Yakymchuk et al., 2012; Waffle et al., 2016). Waffle and coauthors (2016) explore

the physical characteristics and rheology of different analog materials to-be-used in centrifuge analog modelling. Among the different possibilities, our experimental program incorporates a material not commonly used previously, Moon Sand™, a polymer/sand mixture suitable to simulate upper crust brittle sedimentary sequences in centrifuge models (Waffle et al., 2016).

We started the modeling series through a simple experimental scenario to investigate the response of this material to shortening under increased gravity fields. Hence, our experimental program involves three series of experiments: a constant thickness cover detached over a frictional base (Series 1), a constant-thickness series underlain by a ductile *décollement* (Series 2) that sets the basis to then perform tapered cover-*décollement* experiments (Series 3). The rationale behind series 1 and 2 is not to revisit the kinematics and structural styles of frictional and salt-detached fold-and-thrust belts, widely known from natural examples (e.g., Hessami et al., 2001; Barnes et al., 2010), sandbox analog (e.g., Liu et al., 1992; Costa and Vendeville, 2002) and numerical modeling (Ruh et al., 2012; Buiter et al., 2016), but rather to set the foundations of orogenic wedging using Moon Sand™. These models are the pillars that sustain more complex models (Series 3) and ensure the reliability of comparison between our results and previous works.

2.2. Material characterization and scaling parameters

Centrifuge analog modeling permits the use of several analog materials to simulate the upper crust rocks, such as the Demco® modelling clay, Dow Corning Dilatant Compound 3179, Crayola® Model Magic and plasticine building microlaminates (Waffle et al., 2016). Microlaminates, for example, simulate successions of clastic and carbonate rocks interbedded with pelitic rocks (Yakymchuk et al., 2012). The Moon Sand™ consists of regular, fine-grained quartz sand coated with polymer and synthetic rubber binders. There are two different kinds of Moon Sand™, regular (density of 1510 kg/m³) and light (density of 600 kg/m³). They are mixable materials and so the density of the layers can be modified mixing different proportions of each type. This allows for horizontal and vertical density variations (a crucial property in gravity-enhanced experiments) within the cover sequence (Santolaria et al., 2016b). Interlayering thin layers of lighter Moon Sand™ within a regular Moon Sand™ sequence also enhances the visibility of the brittle sequence layering in tomodesitometry scans. Moon Sand™ has been proved to be an effective analog of the brittle upper-crust rocks after developing suitably scaled structures, such as folds, thrusts, tensional fractures, and strike-slip faults (Waffle, 2016). In order to go further into the characterization of this material and its suitability for our series of experiments, we performed several shear tests. Regular shear test carried out for quartz sands used in sandbox analog modeling are usually performed under 0–25 kPa normal loads (Schellart, 2000; Ellis et al., 2004), although shear tests for determining mechanical properties of sand also use relatively high normal loads (50, 100, 150 kPa). In our case, shear tests were carried out considering normal loads that emulate the centrifuge force scenario: an 8 mm thick Moon Sand™ layer can exert a normal stress of 125 kPa when accelerated up to 8820 m/s² (898g). Moon Sand™ shear tests exhibited a first stage of viscoelastic deformation, then a plastic strain hardening stage that ends at the peak strength, yield point. As deformation continues, shear strength remains stable (dynamic stable friction) (Fig. 1a). Occasionally, after peak strength, a plastic softening stage may be inferred from the 5 kPa fall in the 200 kPa load curve (Fig. 1a). The correlation between normal and shear stress for different experiments is close to the ideal Coulomb behavior with a cohesion value of 6.4 kPa and an angle of internal friction of 17.3° (Fig. 1b). In spite of showing values lower than those assumed for the upper crust according to Byerlee's law, this behavior is more realistic when considering deeper levels within the crust, semi-brittle materials, high pore pressure or higher geothermal gradients, or in terms of contrast between the upper (brittle) crust and lower (ductile) crust than in the case of sandbox models, where the interface

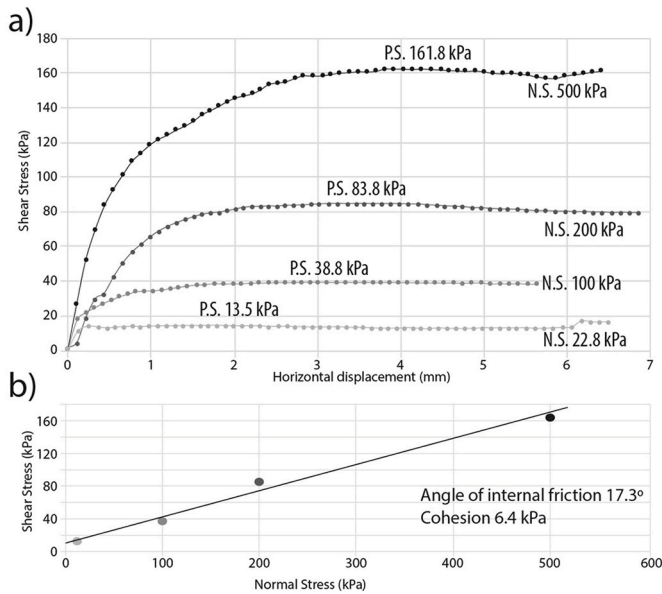


Fig. 1. (a) Shear tests applied to the Moon Sand™ under loads of 22.8, 100, 200 and 500 kPa. P.S., peak strength. N.S., normal stress. (b) Peak strength points projected in a shear stress-normal stress diagram.

between the two layers is responsible for many of the features found in both extensional and compressional settings (see, e.g. Chester, 1995; Kohlstedt et al., 1995; Bos and Spiers, 2002).

Décollement units are here simulated by silicone putty (Crazy Aaron's Thinking Putty™, CATP™) whose density is 1068 kg/m³ (Waffle et al., 2016). To ensure consistency we systematically used green and blue polymers having a density of 1050 kg/m³. At relatively high strain rates (>ca. 10⁻² s⁻¹), this silicone putty shows a strain rate-dependent viscosity (Poulin, 2006; Yakymchuk et al., 2012; Waffle, 2015), and therefore it behaves as a non-Newtonian material. However, at strain rates below ca. 10⁻² s⁻¹, the effective viscosity is constant (Waffle, 2015). Regarding that the estimated experimental strain rates in centrifuge analog modeling are close to 2.5 × 10⁻⁴ s⁻¹, nearly two orders of magnitude below the aforementioned threshold, it can be considered that CATP™ behaves as a Newtonian material whose viscosity is approximately 1 × 10⁻⁴ Pa/s (Yakymchuk et al., 2012; Waffle et al., 2016).

The experimental package lies directly on a plastic sheet that

represents the top of an undeformable basement (Fig. 2). In experiments where a constant-thickness sedimentary sequence is considered (Series 1 and 2), this plastic sheet represents the base of the modelling setup. In experiments considering tapered sequences (Series 3), the plastic sheet lies over a molded basement simulated by Y2 Clay (modeling clay) (Fig. 2). Y2 Clay is a viscoelastic material, with a very high viscosity (<10¹⁰ Pa·s), at shear rates less than 10 s⁻¹ (Waffle et al., 2006). This material is relatively easy to mold when heated but behaves as an elastic solid at room temperature, both under natural gravity conditions or under an applied centrifuge force. Hence, this allows creating a broad range of non-deformable basement geometries simulating, for example, rigid crystalline basements (Waffle et al., 2006).

Models are designed to simulate a simplified fold-and-thrust belt system. To guarantee a reliable comparison between models and nature, the geometry of the models, the mechanical properties of the analog materials and the dynamic and kinematics of experiments were scaled following well-established scaling principles (Hubbert, 1937; Ramberg, 1967a, b, 1973, 1981; Dixon and Summers, 1985; Weijermars et al., 1993) that are summarized in Table 1. The model to nature ratio for length is 1 × 10⁻⁶, which represents that 1 mm in our models is equivalent to 1 km in nature. Since our models are run under enhanced gravity, the model (centrifuge acceleration of 8820 m/s²) to nature (natural gravity, 9.8 m/s²) ratio for gravity corresponds to 898. Being aware of the variability of rock densities in nature, we assumed an average value for the volumetric mass of the sedimentary cover (limestones and siliciclastic rocks) of about 2600 kg/m³, and a mean volumetric mass for salt of about 2200 kg/m³ (e.g., Jackson and Talbot, 1986). Considering the mean density of our analog material, 1510 kg/m³ for the Moon Sand™ and 1050 kg/m³ for the CATP™ silicone putty, the scaling ratio for densities is 0.58 and 0.49 for the sedimentary cover and the salt décollement, respectively. Considering the basic scaling principles, the model to nature ratio for stress σ^* , corresponds to:

$$\sigma^* = \rho^* \cdot g^* \cdot L^*$$

Where ρ^* , g^* and L^* are the model-to-prototype ratio for the density, gravity acceleration, and length. Calculated stresses for models and nature are 1.3 × 10⁴ Pa and 2.55 × 10⁷, respectively.

The strain ratio is calculated from the viscosity ratio (η^*) based on calculation considering variable viscosities of CATP™, ranging from 10⁴ Pa·s (Waffle et al., 2006) and 10⁵ Pa·s (Yakymchuk et al., 2012), and rock salt (10¹⁷–10¹⁹ Pa·s, average = 1018 Pa·s, e.g., Jackson et al., 1994; Van Keken et al., 1993) and the stress ratio σ^* , as follows:

$$\varepsilon^* = \sigma^* / \eta^*$$

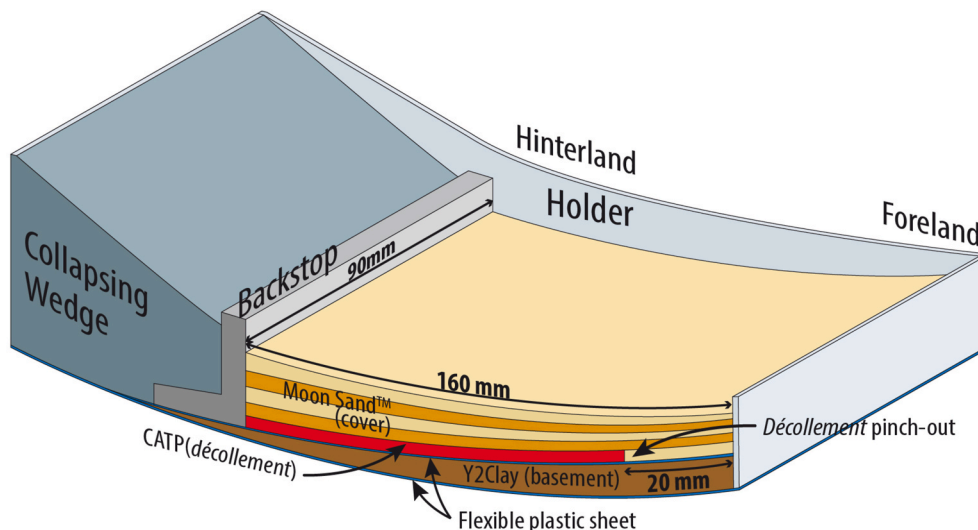


Fig. 2. Experimental setup including the modeled package: Y2Clay forms the basement (brown), CATP, Crazy Aaron's Thinking Putty is the décollement (red) and a color-layered sequence of Moon Sand™ simulates the sedimentary cover (orange and yellow). To the left, the collapsing wedge (blue) pushes the backstop (grey) forward as it flattens under the centrifuge force. (For interpretation of the references to color in this figure legend, the reader is referred to the Web version of this article.)

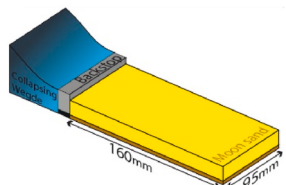
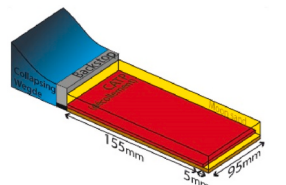
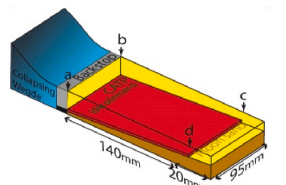
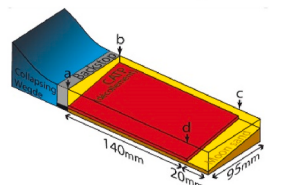
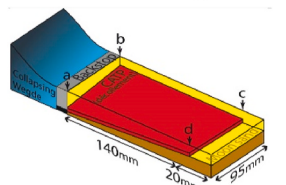
Table 1

Dynamic scaling parameters of the experimental program. The scaling ratio is the model to nature relation of a given magnitude or parameter. * Viscosity of the CATP™ viscous décollement and salt in nature may vary between 1×10^4 Pa-s and 1×10^5 Pa-s and 5×10^{17} Pa-s and 10^{19} Pa-s, respectively. Scaling ratios for the viscosity of the décollement and the strain rate vary accordingly (see text for further details).

Parameter	Equation	Model	Nature	Scaling ratio
Length (L)		1 mm	1 km	1×10^{-6}
Density (ρ)				
Moon Sand™/Sed. Cover		1510 kg/m ³	2600 kg/m ³	0.58
CATP™/Salt décollement		1050 kg/m ³	2200 kg/m ³	0.49
Centrifuge Force/Gravity (g)		8800 m/s ²	9.81 m/s ²	898
Cohesion		6.4×10^3 Pa	5×10^7 Pa	1.3×10^{-4}
Stress (σ)	$\sigma = \rho \cdot g \cdot L$	1.3×10^4 Pa	2.55×10^7 Pa	5.2×10^{-4}
Décollement viscosity (η)		1×10^5 Pa-s *	5×10^{18} Pa-s *	2×10^{-14} *
Strain rate ($\dot{\epsilon}$)	$\dot{\epsilon}$			2.6×10^{10} *

Table 2

Analog models of the experimental program. An asterisk (*) denotes a slight rotation of the backstop leading to differential along-strike shortening. Set-ups are sketched as orthogonal geometries for illustrative purposes, although actual models have curved shapes (see text and Fig. 2 for further details). S, shortening; SC, sedimentary cover; D, décollement; brown, Y2Clay as basement; red, CATP décollement; yellow, layered sequence of colored Moon Sand™; grey, mobile backstop; blue, collapsing wedge.

	Model	S (mm)	SC (mm)/D (mm)	Set-up	
SERIES 1	Model 1.1	65	3/-		
	Model 1.2	65	6/-		
	Model 1.3	61	9/-		
SERIES 2	Model 2.1	65	3/3		
	Model 2.2	70	9/3		
	Model 2.3	62	12/3		
SERIES 3	Series 3.1	Model 3.1.1	60	a: 10.5/1 b:10.5/1 c:1.5/1 d:1.5/1	
		Model 3.1.2	59	a: 10.5/3 b:10.5/3 c:1.5/3 d:1.5/3	
		Model 3.1.3	67	a: 10.5/3 b:10.5/3 c:1.5/1 d:1.5/1	
	Series 3.2	Model 3.2.1	61	a: 10.5/1 b:1.5/1 c:1.5/1 d:10.5/1	
		Model 3.2.2	63-56*	a: 10.5/3 b:1.5/3 c:1.5/3 d:10.5/3	
		Model 3.2.3	62	a: 10.5/3 b:1.5/1 c:1.5/1 d:10.5/3	
	Series 3.3	Model 3.3.1	80	a: 10.5/1 b:1.5/1 c:1.5/1 d:1.5/1	
		Model 3.3.2	75-85*	a: 10.5/3 b:1.5/3 c:1.5/3 d:1.5/3	
		Model 3.3.3	100	a: 10.5/3 b:1.5/1 c:1.5/1 d:1.5/1	

Due to the variability of viscosities, strain rate ratio ranges from 2.6×10^9 and 2.6×10^{12} .

2.3. Design, set-up, and experimental procedure

Our analog models simulate a contractional system detached along a frictional base or a *décollement*. Experiments were carried out at the “Laboratoire de simulation physique, géophysique et numérique” of the INRS-ETE (Québec, Canada) and, in this work, we present a selection of models that represent the culmination of more than 60 initial test models (not illustrated herein) needed to set the proper protocol for building and running centrifuge models using Moon Sand™. This selection includes 15 models which are grouped in three series of experiments. Series 1 involved a horizontal, homogeneous *layer-cake* cover detached on a frictional surface. In Series 2 a similar cover is underlain by a 3 mm-thick CATP™ silicone layer. The *décollement* extends from the backstop to a distal pinch-out and laterally changes to Moon Sand™ to fill the whole length of the models (Table 2). Above it, a layered sequence of colored Moon Sand™ is placed. Tested parameter in Series 1 and 2 are the thickness of the cover (3–9 mm thick in series 1; 3–12 mm thick in series 2, Table 2). Finally, Series 3 consists of models featuring forelandward (Series 3.1), along-strike (Series 3.2) and forelandward-oblique (Series 3.3) tapered covers underlain by a *décollement* (see

Table 2). Within each of these sub-series, the geometry of the cover remains constant while the thickness of the *décollement* varies from constant thickness to tapered geometries (Table 2). The top surface of the models is always flat and horizontal and so the thickness of the *décollement* layer is controlled by the geometry of the Y2 Clay basement. Note that the differential thickness within each model can result in differential loading enhanced by the centrifugal force, in a way similar to differential loading occurring in nature triggering, for example, salt migration in the *décollement* during the compressional evolution of the fold-and-thrust belt.

The deformation box consists of a hard-plastic holder whose dimensions (constrained by the centrifuge rig capacity) are 95 mm wide and 200 mm long. A flexible plastic sheet closes the base of the holder. The modeling package extends 160 mm from the backstop and lies directly on top of the basal flexible plastic sheet (Series 1 and 2) or on top of a Y2Clay basement covered by an extra-flexible plastic sheet (Series 2, Fig. 2). The pinch-out of the *décollement* is located either 155 mm (Series 2) or 140 mm (Series 3, Fig. 2) away from the backstop. In models involving a *décollement* (Series 2 and 3, Table 2), the CATP™ silicone was shaped using automatic (Series 2) or manual (Series 3) rollers. To track the silicone flow, the ductile layer was made by alternating strips of CATP™ silicone of different colors though having similar density and rheology. On top of the basal plastic sheet (series 1) or the *décollement* (series 2 and 3, Fig. 2), the layered regular Moon Sand™ sequence consists of a stack of individual layers of different color allowing to image the internal deformation of models. Colored sands have the same mechanical properties. In Models 3.3.1, 3.3.2 and 3.3.3, layering included thin, density-contrasted, light Moon Sand™ to enhance its visualization in 3D tomodesitometry Scans. These thin layers of light Moon Sand™ do not influence the mechanical stratigraphy of the experimental packages. The coating silicone and rubber binders that link the sand allow handling each layer individually and placing the model in vertical position, as required by the centrifuge rotor. On top of the surface of models, a pattern of circles and, in some cases, lines, were drawn using marker pen ink. To prevent border effects related to the friction between the modeling sequence and the sidewalls, we lubricated this contact by adding CATP™ silicone coats, a technique that is also used in sandbox analog modeling (Costa and Vendeville, 2002; Santolaria et al., 2015).

Models were run in the rotor of a PR-7000 centrifuge, adapted for geological modeling, that rotates at 2000 rpm, which represents a centrifuge force of 898 times the normal gravity acceleration (8820 m/s^2). To assure an even distribution of this centrifuge acceleration, analog models have a curved shape which corresponds to a circumference arc of 57° (given a radius of the centrifuge device of 200 mm). Shortening is accomplished through a Demco® modeling clay wedge that collapses under the centrifuge force (collapsing wedge, Fig. 2) and pushes a rigid backstop that in its turn shortens the modeling package (e.g., Dixon and Summers, 1985; Dixon and Tirrul, 1991; Johns and Mosher, 1996; Harris et al., 2012; Milazzo et al., 2021). The experimental model is shortened in 4–6 stages, each of them lasting 360 s with a run-up time of 60 s and slow-down time of 420 s. During each stage, the amount of shortening is controlled by a linear correlation between the mass of new material added to the collapsing wedge and the horizontal displacement:

$$\text{Shortening} = \text{mass} / (\rho_{\text{DC}} \times A)$$

Where ρ_{DC} is the density of the collapsing wedge material (DowCorning) and A is the area of the backstop.

2.4. Protocol and techniques to analyze the experiments

Quantitative methods for analyzing the ongoing experiments include: i) oblique and top-view step-by-step photographs, and ii) computed tomodesitometry scans allowing 4D characterization of models corresponding to series 3.3 (Models 3.3.1, 3.3.2 and 3.3.3).

Besides, at the end of each experiment, models were serially sliced to better characterize their internal geometry. The use of Moon Sand™ and CATP™ permitted an easy and simple slicing using just a sharp cutting tool which did not require any special model treatment such as freezing, hardening, or watering.

The analysis of oblique and top-view photographs permits to visualize the morphometric evolution of the model and, assisted by the ink pattern drawn on the top of the model, to interpret the location, spacing and lateral extent of structures. This pattern is also used to quantify strain by comparing the final ellipses with their original circular shape (Marques and Cobbold, 2002). In addition, the linear pattern and the orientation of ellipses allows detecting and quantifying vertical axis rotations. Computed tomodesitometry scans (helical X-ray computed tomography also known as CT scanning) is a powerful, non-invasive, visualization technique, that has been proved to be a valuable approach to study the 4D evolution of analog models both in sandbox (e.g., Schreurs et al., 2003; Callot et al., 2012) and centrifuge (e.g., Yakymchuk et al., 2012) experiments. This technique can produce sections in any direction and depth at different stages of the experiment. For further details about X-ray CT scans see Ketcham and Carlson (2001), Mees et al. (2003), and Poulin (2006). Models of series 3.3 we scanned using this technique.

Models of Series 1, 2, 3.1 and 3.2 were serially sliced and documented by high resolution cameras. No CT scans were performed on these models. Serial cross sections allow analyzing the internal architecture of the shortened model, to reconstruct the dominant flow pattern of the *décollement* and to assess layer parallel shortening (LPS) by comparing the final and initial line lengths. From cross-section interpretation, we also carried out a migration-inflation analysis of the *décollement* by comparing the misfit between an idealized planar slab of silicone and its actual areal distribution.

3. Results

3.1. Series 1, frictional thrust wedges

In this series, a layer-cake Moon Sand™ sequence occupies the whole length of the model and no viscous *décollement* is considered. In the three models of this series, upon shortening, a thrust wedge formed, and material is accreted to the thrust wedge in hanging wall sequence as several imbricates (Fig. 3). At the end of the experiment, models display a hinterland characterized by steeply dipping thrusts and backthrusts (Fig. 3b), a thrust wedge consisting of several foreland-verging thrust units and an undeformed foreland. A backthrust develops at the rear part of the model, a typical feature in bi-vergent wedges in sandbox experiments (e.g., Storti et al., 2000, 2001) (Fig. 3c). Beyond the hinterland, the thrust wedge shows forward-verging structures and minor, secondary backthrusts (Fig. 3b). No deformation reached the foreland where layers maintain their original thickness. From the tip of the deformation front to the backstop, the thickness of Moon Sand™ layers progressively increase (Fig. 3b). Critical thrust wedge taper angles attain approximately 10° (Fig. 3b) consistently with relationships between wedge taper and friction angles found in experiments under normal gravity (Gao et al., 2018). LPS attain up to more than 90%. Differences between these models arise regarding the spacing and number of thrusts, and the width of the thrust wedge. The thicker the cover a smaller number of thrusts occur, and the width of the thrust wedge varies from ca. 50 mm, 65 mm and 85 mm in Models 1.1, 1.2 and 1.3, having original stratigraphic thicknesses of 3 mm, 6 mm, and 9 mm, respectively. As in sandpacks models (e.g., Mulugeta, 1988; Liu et al., 1992; Marshak and Wilkerson, 1992; Boyer, 1995; Corrado et al., 1998), an almost linear relationship between the thickness of the brittle cover and the spacing of thrust sheets exists.

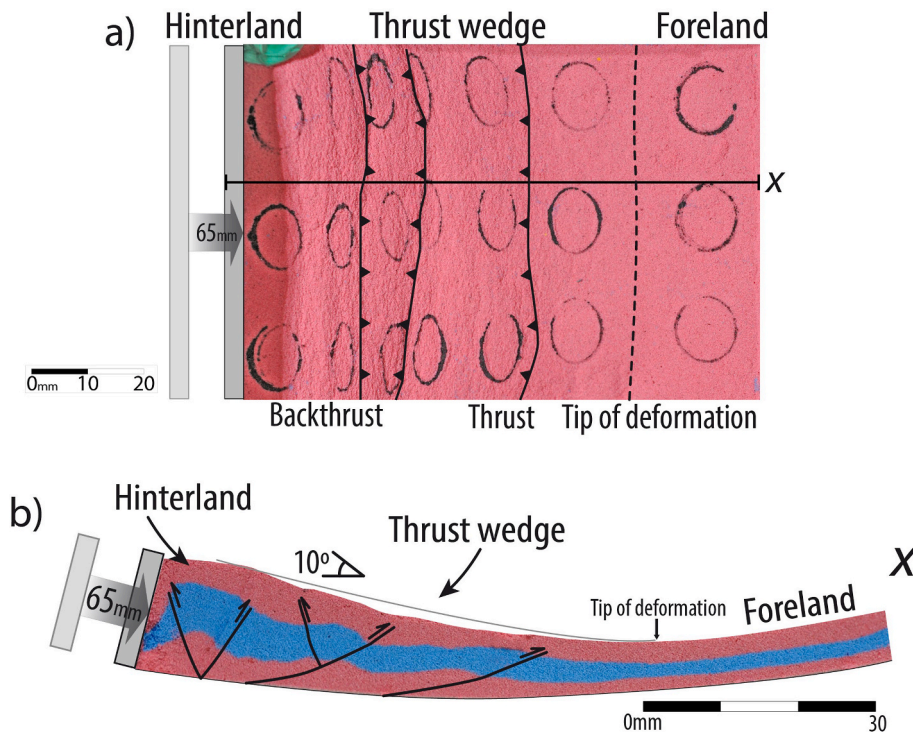


Fig. 3. a), Top-view and b) representative cross-section of Model 1.2 (Series 1, Table 2) at the end of shortening.

3.2. Series 2, “salt”-detached, layer-cake thrust wedges

Series 2 involves models characterized by a layer-cake stratigraphy in which Moon Sand™ lays over a viscous *décollement* made of CATP™. In Models 2.3 and 2.2, shortening is accommodated by the formation of a series of box-folds that occasionally evolve into thrusts (Fig. 4a and b) and a frontal thrust (Model 2.2, Fig. 4b). Conversely, in Model 2.1 (Fig. 4c), where the cover is significantly thinner with respect to the other models and in relation to the *décollement*, the structural style is characterized by an uneven distribution of the contractional

deformation: isoclinal folds with steeply dipping to overturned flanks are localized towards the foreland while a broadly subhorizontal panel lying on top of an inflated *décollement* occurs in the hinterland. The number of structures increases with decreasing cover thickness (Fig. 4). Contrasting with models of Series 1 (frictional thrust wedges), models of Series 2 do not show a dominant vergence and display very low taper angles ($<1^\circ$, Fig. 4).

LPS can be calculated in each case from the deformation of the originally circular markers on the top of the model and the line-length analysis of cross-sections. LPS is strongly dependent upon the sedimentary cover/*décollement* (SC/D) thickness ratio, being higher in the case of thicker covers: Models 2.1, 2.2 and 2.3, with ratios of 1, 3 and 4, register LPS values of 1%, 17% and 58%, respectively.

3.3. Series 3, tapered “salt”-detached thrust wedges

Upper surface views of models with a forelandward cover thinning (series 3.1, Table 2) showing the mobilized salt contour map and the representative section of Model 3.1.3 are shown in Fig. 5a, b and c, respectively. A frontal thrust with significant displacement, nucleated at the *décollement* pinch-out, accommodates most of the shortening (Fig. 5c). Migration of the *décollement* towards the foreland accompanies the progressive translation of this frontal thrust (Fig. 5b). In the hinterland, a gentle anticline cored by the *décollement* layer formed close to the backstop. This structural style and migration patterns characterize all models with forelandward thinning covers regardless of the thickness (Model 3.1.1 vs Model 3.1.2, Table 2) or the geometry of the *décollement* (Model 3.1.2 vs Model 3.1.3). Measured LPS is approximately 19% (Model 3.1.3).

Experiments of Series 3.2 are represented by Model 3.2.3 (Fig. 6). Along-strike thickness variations entailed significant lateral changes in the structural style of the “salt”-detached thrust wedges; thicknesses (and thickness ratio) of the *décollement*-cover sequence controlled the number of structures (Fig. 6a and b) and the amount of displacement at the frontal thrust (Fig. 6c). Where the *décollement*-cover sequence is thickest, two gentle anticlines or box-folds formed (Fig. 6c, “y” section), whereas where the *décollement*-cover is thinnest, up to four folds formed

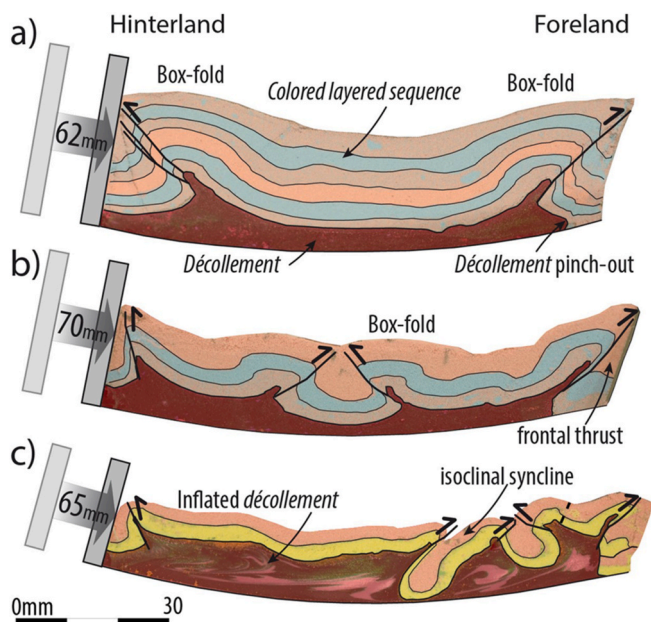


Fig. 4. Representative cross-sections at the end of experiments a) Model 2.3, b) Model 2.2, and c) Model 2.1 (Series 2, Table 2).

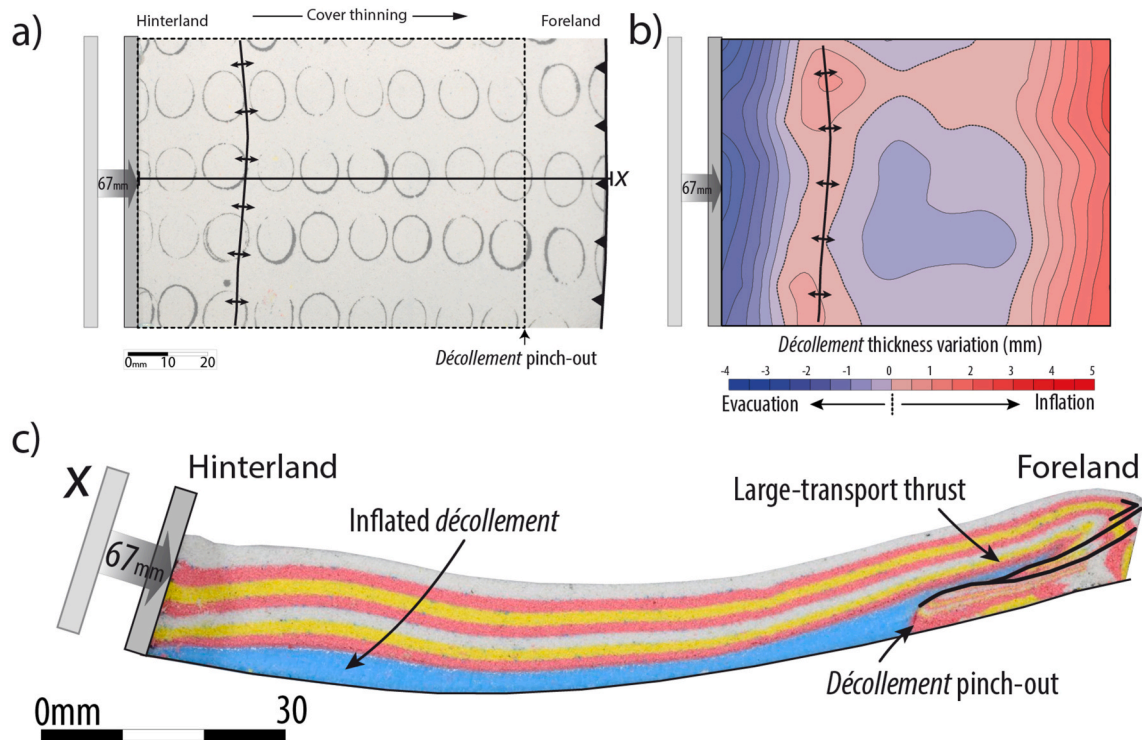


Fig. 5. a) Top-view of Model 3.1.3 (Series 3.1) and b) contour map of the mobilized décollement at the end of shortening; the area of the contour map corresponds to the dashed rectangle in “a”; dotted lines separate areas where décollement evacuates (blue colors) and inflates (red colors). c) representative cross-section of the model. The trace of the section is indicated by the x label in “a”. (For interpretation of the references to color in this figure legend, the reader is referred to the Web version of this article.)

(Fig. 6a, “x” cross-section). Half of these structures propagated laterally showing a curved shape in plan-view and others merged or died out along strike. This curved shape is associated with counterclockwise vertical axis rotations of to 27° (Fig. 6a). Along-strike differential displacement of the frontal thrust resulted in an arc-shaped front. As occurring in models with forelandward thinning of the décollement-cover sequence, the décollement accumulated in the core of anticlines. Another diagnostic feature of models showing along-strike thickness variations was the lateral migration of the basal décollement from thicker cover to thinner cover sectors (Fig. 6b). This effect is enhanced when the décollement is thicker (Model 3.2.2) and when it shows a pre-contractional lateral thinning in the same sense as the cover (Model 3.2.3). In these models, LPS also varies along strike being approximately 31% and 39% from the thin to the thick décollement-cover areas.

The 4D structural evolution of the 3D tapered models (Series 3.3) is illustrated, stage by stage, by top-views, CT scan sections and mobilized décollement contour maps of Model 3.3.3 (Table 2, Fig. 7). At the onset of contraction (Fig. 7, Stage 1), shortening is mostly accommodated by LPS with the exception of incipient folding of the cover along the thinner décollement-cover area (CT scan section, x1, Fig. 7). Traverse décollement migration occurs from the thicker décollement-cover area towards the hinterland, close to the backstop (mobilized contour map in Stage 1, Fig. 7). After 42 mm of shortening (23%), deformation is differentially distributed: (i) along the thinner décollement-cover area, shortening is mainly accommodated by a set of five folds (structures labelled 1 to 5, Fig. 7, Stage 2), depicting a structural spacing of about 11 mm, whereas (ii) along the thicker décollement-cover area a single frontal thrust develops (structure labelled 7, Fig. 7, Stage 2). This frontal thrust, together with its related hanging wall anticline (structure labelled 6, Fig. 7, Stage 2), extends laterally and dies out close to the thinner décollement-cover area, where a gentle anticline occurs on top of the décollement pinch-out (Fig. 7, CT scan section $\times 2$ and y2). Along the thinner décollement-cover area, passive black ink markers reveal up to 10° of counterclockwise

vertical axis rotation. At this time, décollement migrates centrifugally from the center of the thrust wedge and the thicker décollement-cover area towards the hinterland, the foreland and the thinner décollement-cover area. This migration trend prevails until the end of the experiment (see mobilized décollement contour maps in Fig. 7, Stages 2–4). Along the thicker décollement-cover area, further shortening (Stage 3, Fig. 7) is still accommodated by the frontal structure, that consists of two thrusts nucleated at the décollement pinch-out (CT scan section y3, Fig. 7, Stage 3). In the opposite side of the model, folds amplify, and new structures form (labelled 8 and 9, top view and CT scan section x3, Fig. 7, Stage 3). These newly formed structures are more closely spaced (about 6 mm) than the previous ones. Some of the structures extend along strike from the edge to the center of the model and the curvature of surficial traces amplified, displaying counterclockwise vertical axis rotations up to 23° (top view, Fig. 7, Stage 3). Broadly, the inflexion line where structural trends oriented perpendicular to shortening switch to oblique trends is located in the middle of the models, where the SC/D ratio is ca. 6/2. Counterclockwise vertical axis rotations also vary across-strike: distal structures, especially the frontal thrust, display larger values of vertical axis rotation than proximal structures, such as the hinterland-most anticline which is nearly parallel to the backstop. From 65 to 82 mm of shortening (45%) (Stage 4, Fig. 7), in the thicker décollement-cover area, the frontal thrust system still advances while gentle folds finally form behind it as out-of-sequence folding (label 11, top view and CT scan section y4, Fig. 7, Stage 4). In the thinner décollement-cover area, a frontal thrust finally forms, folds amplify, becoming isoclinal and are eventually truncated by break-thrusts (CT scan section x4, Fig. 7, Stage 4). Increasing shortening results in the along-strike growth of structures, the increase of the top view curvature, where structures in the thinner décollement-cover area attain counterclockwise vertical axis rotations of 36° .

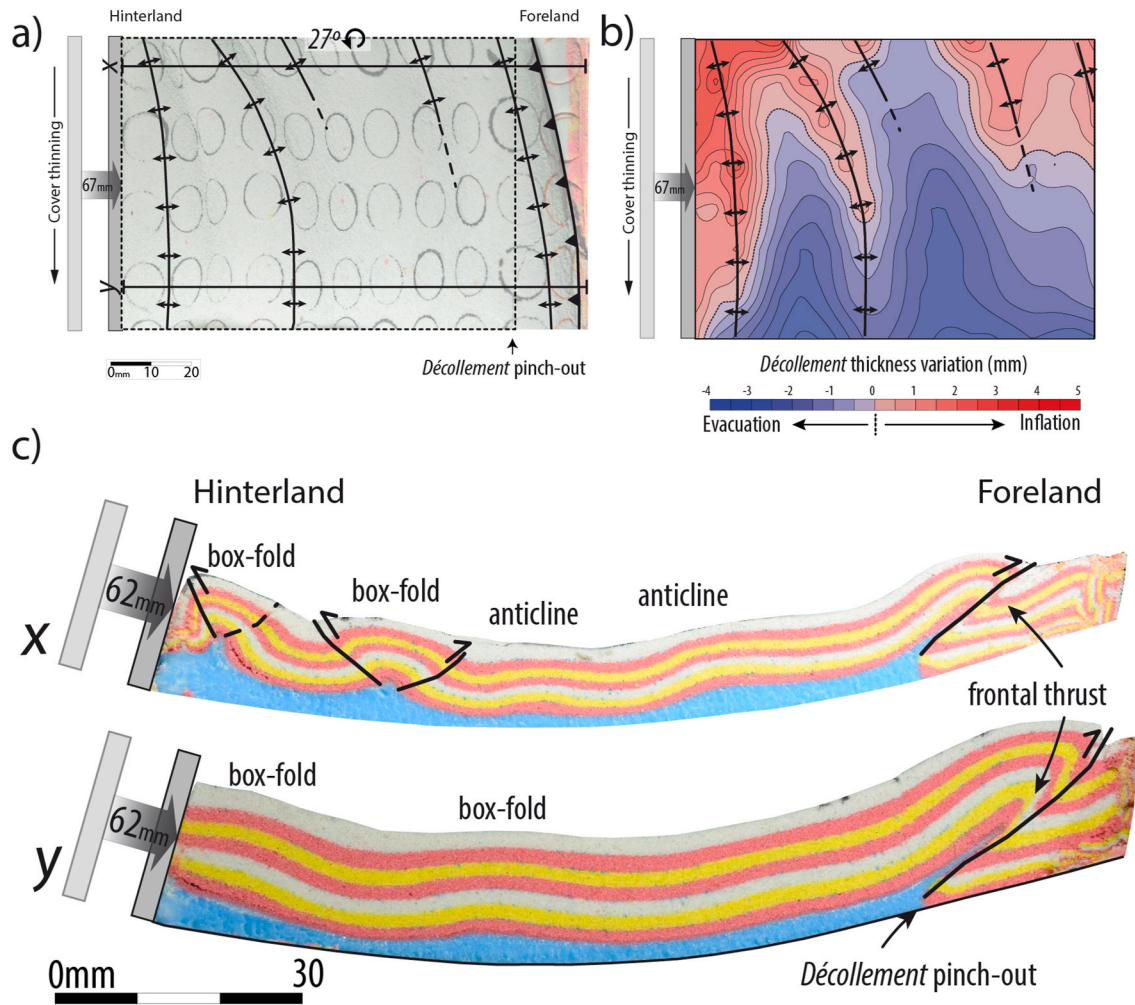


Fig. 6. a) Top-view of Model 3.2.3 (Series 3.2) and b) contour map of the mobilized décollement at the end of experiment; the area of the contour map corresponds to the dashed rectangle in “a”); dotted lines separate areas where décollement evacuates (blue colors) and inflates (red colors). c) representative cross-sections of the model: “x” section involves a thinner décollement-cover couple than “y” section. The trace of the sections is indicated by x and y labels in “a”’. (For interpretation of the references to color in this figure legend, the reader is referred to the Web version of this article.)

3.4. Summary

The characteristics described separately in models with forelandward thinning (Series 3.1) and along-strike (Series 3.2) décollement-cover thickness variations converge in the 3D-tapered models (i.e. including both forelandward and lateral thinning; Series 3.3). Some of these features, such as the changes in the number of structures and the differential displacement along strike for each one is enhanced, thus promoting structures with a higher curvature in plan-view and stronger vertical-axis rotations (36° in Model 3.3.3, and 27° in Model 3.2.3, Figs. 7 and 6 respectively). Vertical axis rotations are not the result of boundary effects (e.g., friction between model and walls because i) the lateral edges of the model are lubricated using CATP™ and ii) there are no vertical axis rotations in the area with thicker layers (Fig. 6a) (where, in addition, more friction might be expected since there is a larger area of contact between model and walls). The 4D analysis of 3D tapered models shows significant differences in their evolution. A break-back sequence is developed in the thicker portion of models due to the early nucleation of the frontal thrust at the décollement pinch-out. Meanwhile, the thinner sector is characterized by a combination of a prevailing break-forward sequence and synchronous thrusting and folding (Fig. 7). In general, for all tapered décollement-cover wedges, both the wavelength of folds and the displacement of the frontal thrust increase with increasing cover thickness. Folds form without a dominant

vergence, with exception of the anticline associated with the major frontal thrust. As shortening progresses, folds become tighter and, some of them develop thrusts in their cores (Fig. 7). Décollement mobilization is due to two kinds of processes: (i) “long-distance” forelandward and/or lateral migration depending on the differential cover load and (ii) accumulation in the core of short-wavelength anticlines (“short-distance” migration from beneath the synclines to the core of the anticlines) in the thinner sectors of the models.

4. Discussion

4.1. Rheology of the Moon Sand™ and resulting structural styles

Shear stress analyses indicate that Moon Sand™ has a nearly ideal Coulomb behavior showing viscoelastic rheology prior to brittle failure. As previously pointed out by Waffle and coauthors (2016), and further investigated in this work, Moon Sand™ represents an ideal analog material to simulate deformation of the upper crust in centrifuge analog models since it captures the localized failure of rocks at shallow levels and at the same time it is able to reproduce the elastic and viscous phenomena that contribute to deformation prior to failure under progressive deformation (Reber et al., 2020). This mixed behavior may result from the mixture of sand, as a granular and brittle material and the coating polymer, as the viscous phase, as it occurs with other mixed

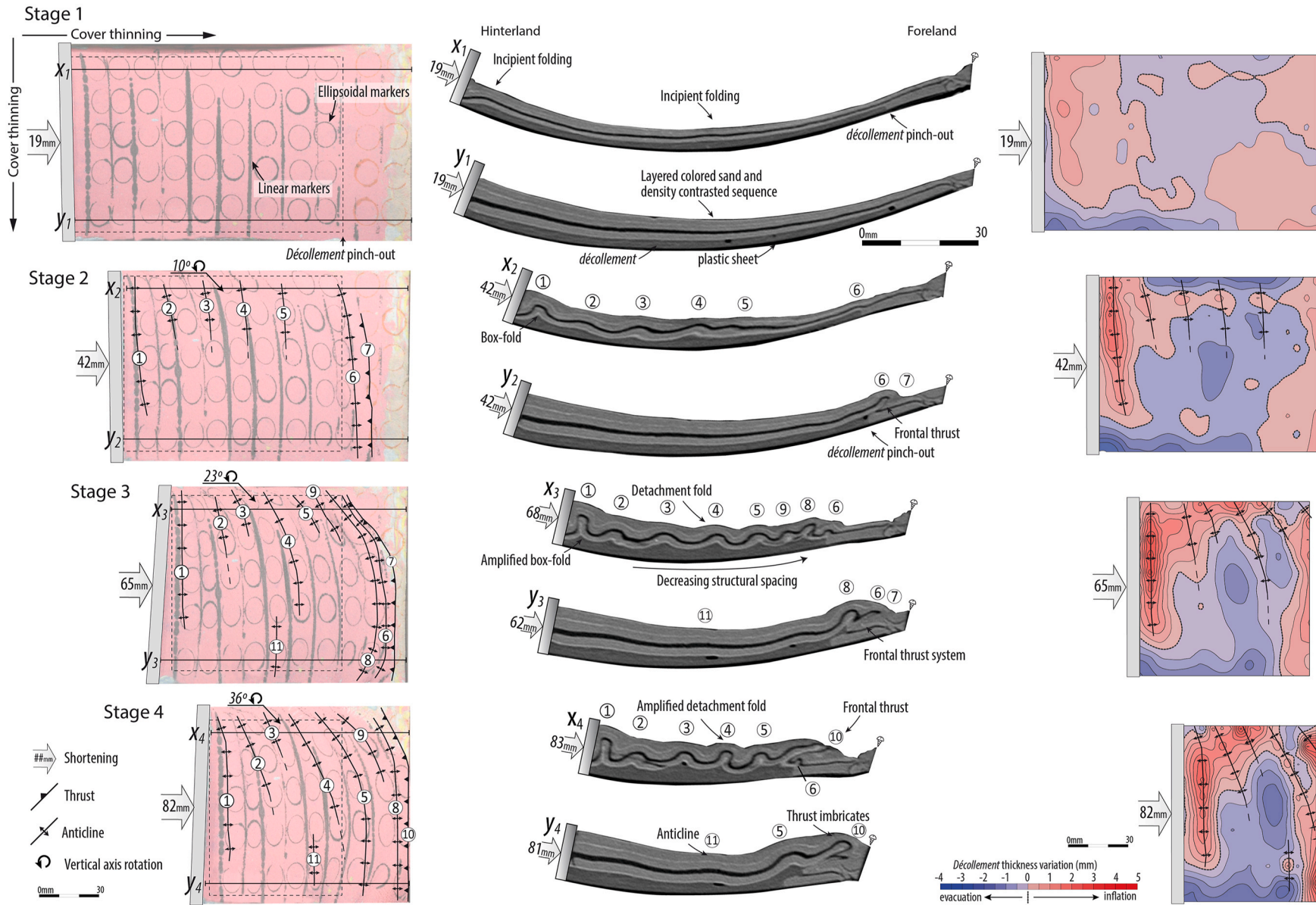


Fig. 7. Evolution of Model 3.3.3 illustrated by top views (left columns), CT scan of the thinner (upper slice, labelled as “x#”) and the thicker (lower slice, labelled as “y#”) décollement-cover areas (central columns) and contour maps of the mobilized décollement (right column). Contour maps have the extension limited by a dashed rectangle in the top views. A dotted line represents the limit between areas where décollement evacuates (blue colors) and inflates (red colors). Structures are mapped after CT Scans interpretation (left and right columns) and numbered (left and central columns) for correlation purposes; numbers do not refer to emplacement chronology. (For interpretation of the references to color in this figure legend, the reader is referred to the Web version of this article.)

material (e.g., Carbopol gels, Piau, 2007; Shafiei et al., 2018; paraffin oil-soaked sand, Corti, 2004). The possible drawbacks of using this material are (i) its mixed brittle-viscous behavior that allows for relatively strong LPS to occur before actual compressional structures develop and (ii) the lower contrast of properties with the lower, ductile level. The first issue apparently makes more difficult to compare our centrifuge models with models in which the upper crust shows a brittle behavior, according to Byerlee's law. The second potential issue ensues stronger differences between our models and "classical" sandbox analog models, in which there is an extremely sharp contrast between the brittle and ductile levels (e.g., Davy and Cobbold, 1991; Costa and Vendeville, 2002). However, the properties of the Moon Sand™ do not necessarily represent conditions farther from natural cases. In fact, ductile-equivalent deformational conditions (e.g., volume loss through pressure solution and/or porosity reduction) are found in the upper crust. This issue is particularly interesting because LPS is actually being recognized as a significant process (often neglected) in fold-and-thrust belts (see, e.g., Sans et al., 2003; Weil and Yonkee, 2012). In many cases, only indirect techniques, such as the Anisotropy of Magnetic Susceptibility can give an account (always difficult to quantify) of the LPS (see, e.g., Gracia-Puzo et al., 2021 and references therein). This can be a complex process during which LPS in its turn interferes with the process of volume reduction due to compaction under sediment load conditions. The lithological conditioning can be also very strong (i.e., early lithification in limestones) in whose case LPS is achieved by means of brittle deformation (Branellec et al., 2015). The lithological factor also relates to the gradual vs. sharp rheological change in centrifuge and sandbox models, respectively. In this sense, each type simulates different mechanical stratigraphies (e.g., shale-dominated basins vs. limestone-dominated basins) that can be applied to different scenarios in terms of pre-orogenic basin formation and evolution.

On the other hand, this new material allows for working under enhanced gravity conditions and this opens up the possibility of studying the migration of the décollement ductile materials within the frame of the kinematic evolution of thrust wedges, a process that is very difficult to observe in conventional sandbox models, partly because of the lower deformation rates and partly because of the high rheological contrast in sand/silicone systems. The viscous-brittle combined behavior of Moon Sand™ led to a distinctive structural style characterized by the occurrence of a broad range of fold geometries, such as long-wavelength and gentle to isoclinal folds with subvertical fold axes (Fig. 8a and b), and box-folds (Fig. 8c). Besides, this behavior allows the simulation of

active, buckle folding (Yakymchuk et al., 2012), what adds a new perspective and possibilities to the already existing, rich and fruitful catalog of brittle structures such as fault-related folds formed in sandbox analog models (e.g., Costa and Vendeville, 2002; Bahroudi and Koyi, 2003; Bonini, 2007). In this sense, our centrifuge models can be considered as a complement to the existing sandbox models simulating similar pre-compressional scenarios. Interestingly, the response of our models to lateral shortening can be also considered under the theory of folding in viscous behavior: the wavelength and number of structures obtained fit predictions from Biot-Ramberg's theory (see Ramsay, 1967 and references therein). This is related with mechanisms of deformation and opens the possibility of working under different conditions in relation to sandpacks, thus completing the set of factors controlling deformation (see e.g., Storti et al., 2007). In this sense, in our models we obtain different fold geometries that can be compared with the ones obtained in sandbox, for example, fault-related box-folds (e.g., Costa and Vendeville, 2002) over detachment folds, which, on the other hand, are actually a common feature in salt-detached contractional systems (Rowan, 1997; Poblet et al., 1998; Schärer et al., 2004; Scott Wilkerson et al., 2007; Izquierdo-Llavall et al., 2018). In our opinion, both types of models must be compared to obtain a realistic picture of geological structures, here considering the geometric and kinematic points of view.

In sandbox analog modeling, detachment folding occurs upon specific conditions such as low cover-décollement thickness ratios (e.g., Bonini, 2003; Duerto and McClay, 2009) or a certain amount of syn-contractional sedimentation that sustains fold amplification (Bonini, 2003; Pichot and Nalpas, 2009; Pla et al., 2019). Similarly, by using Moon Sand™, buckle and detachment folds occur where low cover-décollement thickness ratios exist (Fig. 8d). Nevertheless, conversely to sandbox analog models, fold amplification does not require syn-contractional sedimentation because folding conditions are more easily fulfilled (Fig. 8e). Apart from folding, thrusting mainly occurs along the frontal structures, where (i) single large transport thrusts (Fig. 8f) or (ii) thrust imbricates (Fig. 8g) nucleate at the model salt pinch-out, which represents a notable velocity discontinuity within the model. Minor thrusts and backthrusts also appear at the limb of certain box-folds (Fig. 8c) or as break-thrust (Fig. 8e).

4.2. Centrifuge analog models; basic wedge dynamics, comparison with experiments under natural gravity conditions

In this section, our results are compared with previous frictional and

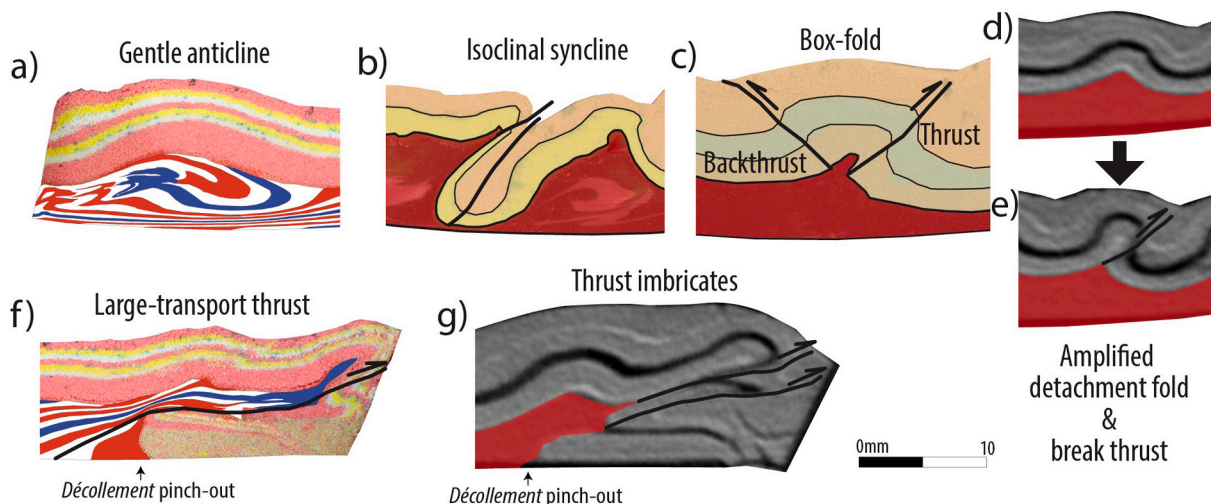


Fig. 8. Representative structural features of 3D tapered cover models (series 3). a) gentle detachment anticline cored by the décollement layer (blue, white and red layers) depicting ductile-deformed recumbent folds (Model 3.3.2); b) isoclinal syncline in Model 2.1; Box-fold in Model 2.2; d) detachment fold subsequently e) amplified and truncated by a break-thrust; f) large-transport thrust detached along a strongly sheared décollement (blue, white and red layers; Model 3.3.2); g) thrust imbricates in Model 3.3.3. (For interpretation of the references to color in this figure legend, the reader is referred to the Web version of this article.)

non-frictional thrust wedge experiments involving brittle and ductile-brittle stratigraphy and run under natural and enhanced gravity conditions. Centrifuge analog modeling programs involving multilayered sequences based on combining different material such as silicone polymers, plasticines and/or modeling clays (Dixon and Summers, 1985; Liu and Dixon, 1990; Dixon and Tirrul, 1991; Godin et al., 2011; Noble and Dixon, 2011; Yakymchuk et al., 2012; Faisal and Dixon, 2015; Waffle et al., 2016) are out of the scope of this discussion.

Under natural gravity conditions, sandbox analog thrust wedges grow and widen by maintaining a critical taper, and topography is controlled by the angle of internal friction, the cohesion of the cover rocks (almost negligible in sandpicks) and the coefficient of basal friction. This provides powerful insights into the geometry and dynamics of thrust systems and accretionary wedges (e.g., Chapple, 1978; Davis et al., 1983; Dahlen et al., 1984). In this work, experiments presented in Series 1 reached maximum surface slope angle of 10° . This value is in good agreement with those predicted by the critical taper theory (e.g., Davis et al., 1983; Gao et al., 2018). In sandbox analog models, critical taper angles may vary between 1.5° and 18.5° for low (0.37) and high (0.55) basal friction conditions, respectively (e.g., Liu et al., 1992), whereas in centrifuge analog models, they attain ca. 14° or ca. 20° in frictional, damp sand (Mulugeta, 1988) or K-Feldspar sand (Milazzo et al., 2021) thrust wedges, respectively. Thrusting in relatively narrow and limited zones dominates in frictional sandbox thrust wedges (e.g., Liu et al., 1992; Lohrmann et al., 2003; Storti et al., 2000; Agarwal and Agrawal, 2002; Soto et al., 2003; Granado et al., 2017, among many others) and in centrifuge analog models involving K-Feldspar sands (Milazzo et al., 2021). Conversely, in our centrifuge analog models underlain by a frictional detachment, deformation is mostly accommodated by thickening of thrust sheets. Such thickening is likely related to the combined viscous-brittle rheology of Moon Sand™.

The occurrence of basal low-strength décollements, such as salt in nature or silicone polymers in analog modelling, leads to very low taper angles (e.g., Davis and Engelder, 1987; Cotton and Koyi, 2000; Costa and Vendeville, 2002). This is also observed in our experiments of Series 2 and 3 (i.e., décollement-detached thrust wedges), where surface slope angles range between 0° and 2° . The following common features observed in sandbox models developed under normal gravity conditions and above ductile décollements (e.g., Davis and Engelder, 1987; Letouzey et al., 1995; Cotton and Koyi, 2000; Costa and Vendeville, 2002; Bahroudi and Koyi, 2003; Luján et al., 2003, 2006) coincide with those observed in our centrifuge models (i.e. Series 2 and 3; Figs. 4–7): (1) rapid localization of the outer deformation front along the distal pinch-out of the basal décollement, (2) lack of a dominant vergence in contractional structures, (3) thrust nucleation that does not follow a simple sequence and synchronous thrusting in different parts of the model, and (4) thickening of ductile décollement material in the cores of the anticlines. Our results portray how the thickness of the décollement plus that of the cover sequence are a first order controlling factor of the structural spacing and the number of structures that accommodate shortening: thinner sequences promote the formation of a higher number of structures which are narrowly spaced and show shorter wavelengths than thicker sequences. This observation is true whether different thicknesses are tested separately (series 2, Fig. 4) or progressive variations of thicknesses occur in a single experiment (series 3, Figs. 6 and 7). These features agree with previously published works for frictional and frictional-viscous sandbox analog wedges (Huiqi et al., 1992; Marshak and Wilkerson, 1992; Smit et al., 2003; Storti et al., 2007; Santolaria et al., 2015; Borderie et al., 2019).

Bed-length analysis permits to estimate the amount of LPS in our models, by comparing the initial and final length of a given stratigraphic horizon. In the sand layers of models run under normal gravity conditions (Mulugeta and Koyi, 1987; Koyi, 1995; Koyi and Vendeville, 2003), LPS is accommodated by volume loss through porosity reduction. In frictional sandbox models, LPS has been estimated to accommodate between 17% and 41% of the total shortening (Koyi and Vendeville,

2003). However, in the presence of a viscous basal décollement, LPS is significantly reduced (Koyi and Vendeville, 2003). In centrifuge analog models using plasticine and silicone putty as analog materials, Liu and Dixon (1990) already observed that LPS accounts for half of the total of shortening. In our centrifuge experiments performed with Moon Sand™, we have observed that LPS can accommodate higher amounts of deformation: over 90% of the shortening is accommodated by LPS in frictional Models 1.1 and 1.2, in which very few structures actually formed. LPS decreases in models of series 2 and 3.2, where a positive correlation between the cover-décollement ratio and shortening accommodated by LPS is found. Thicker covers (Model 2.3, Fig. 4a) attain up to 58% of LPS while thinner covers (Model 2.1, Fig. 4c) do not register significant figures ($<1\%$). This is likely related to the increase of strength with depth (i.e., with cover thickness). Upon contraction, in those models considering a pre-contractional, forelandward-thinning sedimentary wedge (series 3.1), most of the shortening is accommodated by frontal thrusting and LPS reaches ca. 20%. This value increases in those models involving along strike tapered pre-contractional sequences where LPS is differentially distributed: it changes from ca. 19% to ca. 24% between the thinner and thicker parts of the cover, respectively. CT Scans of Model 3.3.3 (Fig. 7) permit to quantify LPS stage-by-stage. The graph in Fig. 9 illustrates the cumulative LPS (normalized with respect to the total shortening of the experiment; solid lines) and the differential LPS at each stage (normalized with respect to the shortening applied at each stage; dashed lines) for the areas with thinner and thicker sequences. Until 42 mm of shortening, cumulative LPS is evenly distributed along the experimental packages and differential LPS values attained approximately between 88% and 79% either in the thicker and thinner décollement-cover areas (Fig. 9). After 42 mm, there is a decrease of the differential LPS from ca. 85% and 88%–57% and 42% in the thicker and thinner décollement-cover areas, respectively. From that point onwards, areas with thicker stratigraphy kept on accumulating slightly larger amounts of LPS than areas with thinner sequences. In the thinner sequence area, differential LPS drops to 5% (Fig. 9) coinciding with initiation of the frontal thrust, since most of the shortening is accommodated by forward translation of the cover.

4.3. Influence of pre-deformational lateral taper in fold and thrust belts

The occurrence of a gentle pre-deformational lateral taper appears as a fundamental parameter controlling the architecture of décollement-bearing thrust wedges. In models of series 3.1, the forelandward thinning led to a rapid transfer of deformation to the distal décollement pinch-out and most of the shortening is accommodated by a large-transport thrust in the frontal thrust wedge. Then, evolution of the thrust wedge is limited to the frontal translation of an undeformed cover

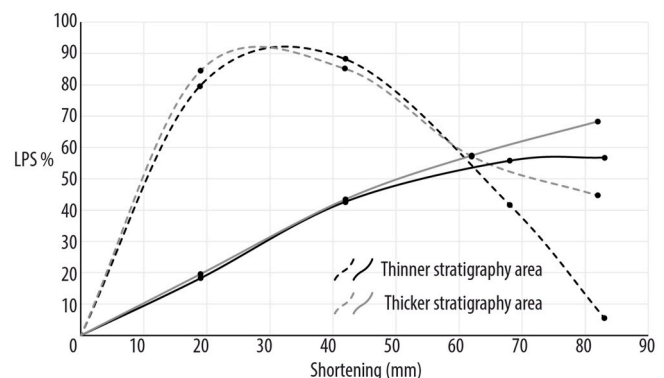


Fig. 9. Graph displaying the cumulative layer parallel shortening (normalized with respect to the total shortening of the experiment) (solid lines) and the differential LPS at each stage (normalized with respect to the shortening applied at each stage) (dashed lines) for the areas with thinner and thicker sequences, black and grey lines respectively, of Model 3.3.3.

pack. It is not until close to the end of experiments when the cover pack registers some deformation behind the wedge front. Using sandbox analog models, Smit and coauthors (2003) tested pre-shortening configurations geometrically similar to our models of Series 3.1: a forelandwards thinning tapered décollement-cover with an initial angle of 3° . As in our models, at the onset of shortening, deformation localized in the distal décollement pinch-out. But, with further shortening (and opposite to what we observed in centrifuge models) deformation progressively shift backwards and shortening is mostly accommodated by folds and thrusts within the cover instead of its frontal translation as we observed. A lateral and/or oblique cover thinning and/or décollement-cover thinning determines the number and displacement of thrusts and hence the occurrence of oblique and curved geometries in plan-view, similarly to results obtained in sandbox models without a ductile décollement (Soto et al., 2002, 2003). The lateral taper angle also controls the amount of vertical-axis rotation in the cover and the lateral and forward migration of the ductile décollement. Previous sandbox analog modeling experimental programs (e.g., Cotton and Koyi, 2000; Schreurs et al., 2001; Luján et al., 2003; Bahroudi and Koyi, 2003; Vidal-Royo et al., 2009) tested the influence of a discontinuous or geometrically variable ductile décollement overlain by a constant thickness sandpack. In general, these studies reported vertical axis rotation on the cover associated with lateral décollement pinch-outs trending parallel to the shortening direction. Besides, alike in Series 3.2 models, Storti et al. (2007) modeled sand-silicone packs with a lateral sedimentary taper, obtaining qualitatively similar results, except for the occurrence of a first curved feature associated with important vertical-axis rotation and a strike-slip fault system controlled by the lateral décollement pinch-out located at the thinner sector of models. This particular geometrical constraint (lateral décollement pinch-out) is not present in our models and therefore results can be analyzed in terms of a laterally continuous décollement. Therefore, this allows us to conclude that vertical axis rotations are not necessarily related to a lateral velocity discontinuity but just the thinning of the décollement and/or the overlying sedimentary cover.

If we consider our 3D tapered models (Models 3.3.1, 3.3.2 and 3.3.3) in combination with their mirror image (i.e., a pre-orogenic configuration showing a steer's head geometry in the along-strike section, Fig. 9), they would depict a salient characterized by (i) opposite vertical axis

rotation of structures at both sides, and (ii) outward migration and backwards accumulation of the décollement (Fig. 10). Salient (Miser, 1932) is used as a descriptive geometrical term that refers to an arcuate (convex toward the foreland) feature of an orogenic system and it has not any kinematic implication as for example, orocline (Carey, 1955), that corresponds to an orogenic system that has been flexed. Salients occur in many fold-and-thrust belts (Macedo and Marshak, 1999) and their origin may be controlled (Weil and Sussman, 2004 and references therein) by: i) pre-deformational thickness variations and the presence of basal décollements (Beutner, 1977; Allmendinger et al., 1990; Lawton et al., 1994; Boyer, 1995; Mitra, 1997; Sempere, 1995), ii) the geometry of the underlying basement or hinterland indenter (Marshak, 2004), iii) buttress effects, iv) wrench-faulting and v) significant changes of the regional stress-field (Weil et al., 2000, 2001). Among all these factors, the presence of salt detachments has been interpreted to play a role on the development of salients in the Jura Mountains (Western Alps, Becker, 2000; Hindle et al., 2000; Hindle and Burkhard, 1999), the Monterrey salient (northeastern Mexico, Scott Wilkerson et al., 2007), and the Zagros (SW Iran, Bahroudi and Koyi, 2003; Callot et al., 2012; Snidero et al., 2020), among others. In the following section, we explore the importance of the pre-contractual architecture during mountain building in the well-known example of the South-Central Pyrenees and make comparisons with our experimental results.

4.4. Validation with nature; the South-Central Pyrenees

The South-Central Pyrenees display a south-verging arched shape in map view. In its central part, structures trend parallel to the tectonic grain of the range ($\sim N120E$) while, when approaching its eastern and western boundaries, lateral structures strike highly oblique to the Pyrenean trend, thus defining a fold-and-thrust belt salient (Sussman et al., 2004; Muñoz et al., 2013, 2018, Fig. 11). The South-Central Pyrenees consist of three main thrust sheets which were emplaced from Cretaceous to Oligocene times, mainly following a piggyback thrust sequence. These thrust sheets are, from North to South (older to younger): the Cotiella-Bóixols, the Peña Montañesa-Montsec and the Gavarnie-Sierras Exteriores thrust sheets (Muñoz et al., 2013 and references therein). The thrusts root in Triassic evaporites that (i) represent the regional décollement and (ii) extensively crop out as salt accumulations and

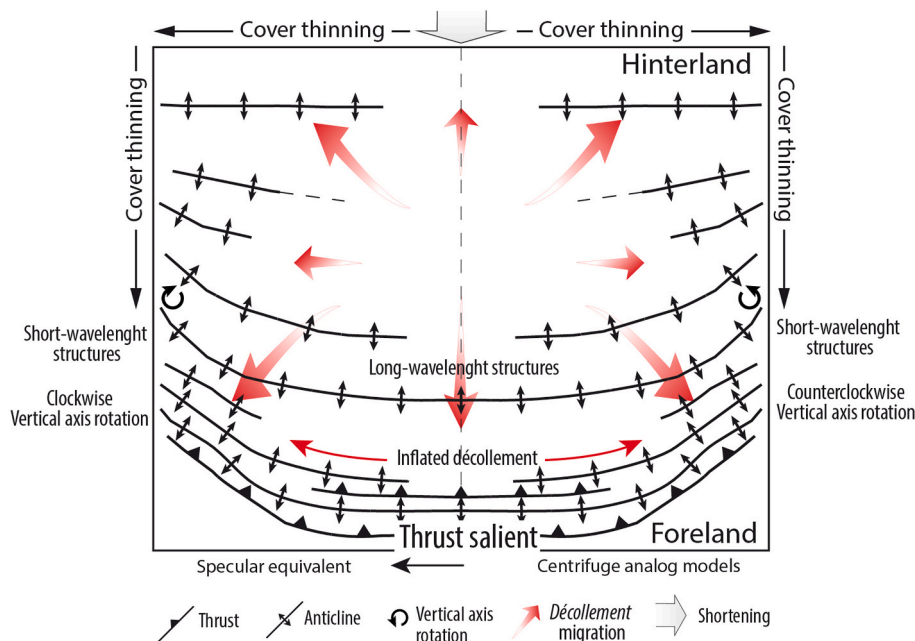


Fig. 10. Sketch that summarizes the structural style found in 3D tapered décollement-cover Model 3.3.3. Our results represent one half of this sketch, the other half has been completed with its mirror image for the sake of comparison with the South Central Pyrenean salient (see section 4.4).

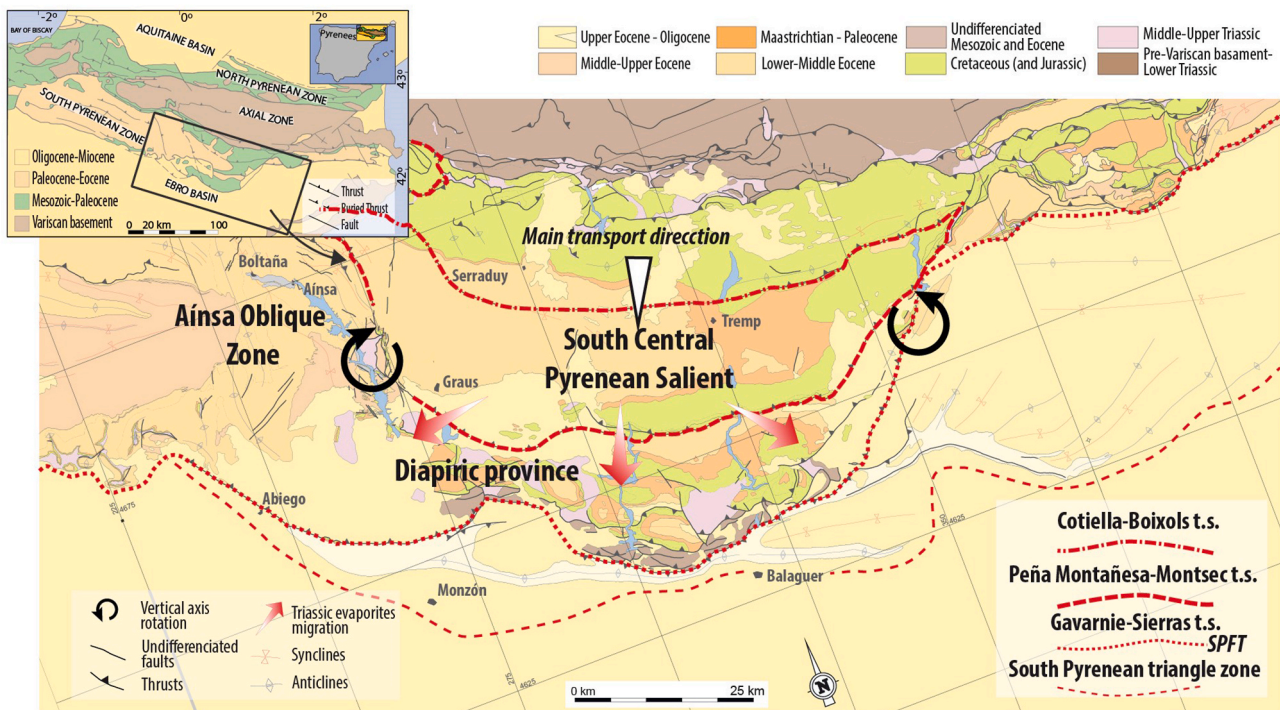


Fig. 11. Simplified geological map of the South-Central Pyrenees where the main thrust sheets are displayed (see top-left corner for regional location). Note their curved shape as well as the orientation of central to lateral structures. Modified from Santolaria et al. (2020), after Muñoz et al. (2018).

diapirs in the northern boundary of this salient and along the southernmost thrust sheet where these bodies are related to an inflated Triassic salt horizon (Santolaria et al., 2014, 2016a).

The pre-contractual stratigraphic succession in the South-Central Pyrenees (Mesozoic in age) depicts a significant southward thinning, from more than 5000 m in the Cotiella-Boixols thrust sheet to less than 300 m in the South-Pyrenean front, i.e., the southern edge of the Gavarnie Sierras-Exteriores thrust sheet (Fig. 11). A less abrupt, along-strike thinning also occurs from the East to the West (Soto et al., 2002). In its turn, the Triassic *décollement* thins dramatically or disappears towards the lateral edges of the orogenic salient (Muñoz et al., 2013). It is in these edges where oblique structures occur. To the East, the structures related to the eastern edge of the salient strike N030E whereas, to the West, in the Ainsa Oblique Zone (Fernández et al., 2012; Muñoz et al., 2013), a series of N-S trending anticlines crop out, forming part of the Gavarnie-Sierras Exteriores thrust sheet. This oblique trend is not primary. Paleomagnetism reveals that these structures were emplaced with a subtle obliquity (Mochales et al., 2012; Muñoz et al., 2013) and then they underwent slight counter-clockwise vertical axis rotations in the eastern boundary (Dinarés-Turell, 1992) and high (up to 80°) clockwise vertical axis rotations in the Ainsa Oblique Zone (Fig. 10) during Eocene-Oligocene times (Bentham, 1992; Sussman et al., 2004; Mochales et al., 2012; Beamud Amorós, 2013; Muñoz et al., 2013). According to paleomagnetic data and seismic, well and structural interpretations, the South-Central Pyrenean salient is a progressively formed arc with divergent thrust transport directions formed due to differential displacement gradients (Sussman et al., 2004; Muñoz et al., 2013, 2018).

All in all, the pre-contractual features in the South-Central Pyrenees are comparable to the models of series 3.3: basin-related initial geometries including along- and across-strike thickness variations of the *décollement* and the overlying sedimentary sequence. Both in South-Central Pyrenees and in our models, this configuration promotes i) the co-existence of structures parallel and oblique to the main trend, ii) an increase in the number of structures and a shorter structural spacing and wavelength towards the edges of the orogenic salient, where the

sedimentary cover is thinner, and iii) the characteristic, overall salient geometry. Besides, the curvature of the South-Central Pyrenean salient has been proved to be secondary, which goes hand by hand with the progressive vertical axis rotation of the oblique structures in its lateral edges. Similarly, in Model 3.3.3 (Fig. 7), between Stages 2 and 4 the linear frontal thrust system progressively acquires a curved shape, at the same time that vertical axis rotation of the innermost structures increases. Furthermore, accumulation of salt and formation of diapirs along the edges of this orogenic salient has been proposed to be partially caused by the outward, centrifugal migration of the Triassic evaporites (Santolaria et al., 2016a), from beneath pre- and syn-contractual depocenters to the areas where the sedimentary cover is thinner. Results obtained by compressing a tapered cover over a *décollement* level, as in series 3.3, support this hypothesis since such an outward migration is also observed in the silicone basal plate (see contour maps of the mobilized *décollement* in Stages 3 and 4 in Fig. 7).

5. Conclusions

Our experimental centrifuge analog modelling program showed that Moon Sand™, and CATP™ (Crazy Aaron's Thinking Putty™) silicone putty, are ideal analog materials for centrifuge modeling to simulate deformation occurring in frictional thrust wedges and salt-detached fold-and-thrust belts. Shear tests indicate that Moon Sand™ behaves as a visco-elastic material prior to brittle failure which makes it a good analog of sedimentary rocks in the brittle upper crust. This combined behavior is likely related to its composition: regular, fine-grained quartz sand coated with polymer and synthetic rubber binders. Upon shortening and when detached along CATP™ silicone putty, deformation results in layer parallel shortening, folding, and thrusting. Detachment folds with box-fold geometry and associated break-out thrusts, and thrusts showing significant displacements dominate the structural style in the presented models.

A series of simple, layer-cake, models successfully tested the use of Moon Sand™ in modeling a frictional scenario (Series 1), where the models grew by incorporating new material to the frontal thrust wedge

attaining taper angles of 10°, values that are in good agreement with those predicted by the critical taper theory. Taper angles drop to 0–2° in *décollement*-detached models (Series 2), as also found in sandbox models and nature. 3D tapered models that demonstrate the influence of lateral thickness variations of the *décollement*-cover pre-contractual sequence showed: i) deformation partitioning triggered differential frontal translation and vertical axis rotation of the cover where it is thinner and ii) along- and across-strike migration of the *décollement*.

The similarities mentioned above justify the comparison between the results obtained from experiments performed under natural gravity conditions and our centrifuge analog models. Both types of models indicate that the pre-orogenic wedging of the sedimentary sequence favors the along-strike change of structural trends, vertical axis rotations and *décollement* migration. Thrust salients and especially progressive arcs in orogenic belts can be understood as a response to progressive changes in thickness of the *décollement* levels and the sedimentary cover without the need of other factors as abrupt *décollement* pinch-outs, along-strike changes in shortening rate or basement geometries. This highlights the strong control imposed by facies distribution and, consequently, paleogeography, on the development and geometry of subsequent structures. This is the case of the South Central Pyrenean salient.

Using conventional centrifuge analog materials together with Moon Sand™ to simulate the semi-brittle cover is shown to be a promising new approach to investigate controlling factors in fold-and-thrust belts.

CRedit authorship contribution statement

P. Santolaria: Conceptualization, Methodology, Investigation, Writing – original draft, Writing – review & editing. L.B. Harris: Writing – review & editing, Methodology, Investigation. A.M. Casas: Conceptualization, Writing – review & editing. R. Soto: Conceptualization, Writing – review & editing.

Declaration of competing interest

The authors declare that they have no known competing financial interests or personal relationships that could have appeared to influence the work reported in this paper.

Acknowledgements

This work was founded by a research grant from the Sobrarbe-Pirineos Unesco Global Geopark, the project KINESAL (CGL2010-21968-C02-02) of the Spanish Ministry of Economy and Competitiveness and a DGA-PhD grant (Aragón Government) to the first author. All experiments were performed in the laboratory for physical, numerical, and geophysical simulations at INRS-ETE, Quebec. CT scanning was undertaken in the Multidisciplinary CT Laboratory for Natural Resources and Civil Engineering at INRS-ETE.

References

- Agarwal, K.K., Agrawal, G.K., 2002. Analogue sandbox models of thrust wedges with variable basal frictions. *Gondwana Res.* 5 (3), 641–647.
- Allmendinger, R.W., Figueroa, D., Snyder, D., Beer, J., Mpodozis, C., Isacks, B.L., 1990. Foreland shortening and crustal balancing in the Andes at 30 degrees S latitude. *Tectonics* 9, 789–809.
- Bahroudi, A., Koyi, H., 2003. The effect of spatial distribution of Hormuz salt on deformation style in the Zagros fold and thrust belt: an analogue modeling approach. *J. Geol. Soc. London* 160, 719–733.
- Barnes, P.M., Lamarche, G., Bialas, J., Henrys, S., Pecher, I., Netzeband, G.L., Greinert, J., Mountjoy, J.J., Pedley, K., Crutchley, G., 2010. Tectonic and geological framework for gas hydrates and coldseeps on the Hikurangi subduction margin, New Zealand. *Mar. Geol.* 272 (1–4), 26–48. <https://doi.org/10.1016/j.margeo.2009.03.012>.
- Beamud Amorós, E., 2013. Paleomagnetism and Thermochronology in Tertiary Syntectonic Sediments of the South-Central Pyrenees: Chronostratigraphy, Kinematics and Exhumation Constraints. Univ. Barcelona, p. 251. PhD Thesis.
- Becker, 2000. The Jura Mountains — an active foreland fold-and-thrust belt? *Tectonophysics* 321 (4), 381–406.
- Bentham, P., 1992. The Tectono-Stratigraphic Development of the Western Oblique Ramp of the South-Central Pyrenean Thrust System, Northern Spain. PhD Thesis. University of Southern California, p. 253.
- Beutner, E.C., 1977. Causes and consequences of curvature in the Sevier orogenic belt, Utah to Montana. In: Heisey, E.L., Lawson, D.E., Norwood, E.R., Wach, P.H., Hale, L.A. (Eds.), *Rocky Mountain Thrust Belt, Geology and Resources: Guidebook for the Wyoming Geological Association Annual Field Conference*, 29, pp. 153–165.
- Bonini, M., 2003. Detachment folding, fold amplification, and diapirism in thrust wedge experiments. *Tectonics* 22, 1065–1103.
- Bonini, M., 2007. Deformation patterns and structural vergence in brittle-ductile thrust wedges: an additional analogue modeling perspective. *J. Struct. Geol.* 29, 141–158.
- Borderie, S., Graveleau, F., Witt, C., Vendeville, B.C., 2018. Impact of an interbedded viscous décollement on the structural and kinematic coupling in fold-and-thrust belts: insights from analogue modeling. *Tectonophysics* 722, 118–137. <https://doi.org/10.1016/j.tecto.2017.10.019>.
- Borderie, S., Vendeville, B.C., Graveleau, F., Witt, C., Dubois, P., Baby, P., Calderon, Y., 2019. Analogue modeling of large-transport thrust faults in evaporites-floored basins: example of the Chazuta Thrust in the Huallaga Basin, Peru. *J. Struct. Geol.* 123, 1–17. <https://doi.org/10.1016/j.jsg.2019.03.002>.
- Bos, B., Spiers, C.J., 2002. Frictional-viscous flow of phyllosilicate-bearing fault rock: micropysical model and implications for crustal strength profiles. *J. Geophys. Res. Solid Earth* 107 (B2), ECV–1.
- Boyer, S.E., 1995. Sedimentary basin taper as a factor controlling the geometry and advance of thrust belts. *Am. J. Sci.* 295, 1220–1254.
- Branellec, M., Callot, J.P., Nivière, B., Ringenbach, J.C., 2015. The fracture network, a proxy for mesoscale deformation: constraints on layer parallel shortening history from the Malargüe fold and thrust belt, Argentina. *Tectonics* 34 (4), 623–647.
- Buiter, S.J.H., Schreurs, G., Albertz, M., Gerya, T.V., Kaus, B., Landry, W., le Pourhiet, L., Mishin, Y., Egholm, D.L., Cooke, M., Maillot, B., Thieulot, C., Crook, T., May, D., Souloumiac, P., Beaumont, C., 2016. Benchmarking numerical models of brittle thrust wedges. *J. Struct. Geol.* 92, 140–177. <https://doi.org/10.1016/j.jsg.2016.03.003>.
- Calassou, S., Larroque, C., Malavieille, J., 1993. Transfer zones of deformation in thrust wedges: an experimental study. *Tectonophysics* 221 (3–4), 325–344.
- Callot, J.P., Trocmé, V., Letouzey, J., Albouy, E., Jahani, S., Sherkati, S., 2012. Preexisting salt structures and the folding of the Zagros Mountains. In: Alsop, G.I., Archer, S.G., Hartley, A.J., Grant, N.T., Hodgkinson, R. (Eds.), *Salt Tectonics, Sediments and Prospectivity*, vol. 363. Geological Society, London, Special Publications, pp. 545–561. <https://doi.org/10.1144/SP363.27>, 2012.
- Carey, S.W., 1955. The orocline concept in geotectonics. *Proc. Royal Soc. Tasmania* 89, 255–288.
- Chapple, W.M., 1978. Mechanics of thin-skinned fold-and-thrust belts. *Geol. Soc. Am. Bull.* 89 (8), 1189–1198.
- Chester, F.M., 1995. A rheologic model for wet crust applied to strike-slip faults. *J. Geophys. Res. Solid Earth* 100 (B7), 13033–13044.
- Corrado, S., Di Bucci, D., Naso, G., Faccenna, C., 1998. Influence of palaeogeography on thrust system geometries: an analogue modelling approach for the Abruzzi-Molise (Italy) case history. *Tectonophysics* 296 (3–4), 437–453.
- Corti, G., 2004. Centrifuge modelling of the influence of crustal fabrics on the development of transfer zones: insights into the mechanics of continental rifting architecture. *Tectonophysics* 384, 191–208.
- Costa, E., Vendeville, B.C., 2002. Experimental insights on the geometry and kinematics of fold-and-thrust belts above a weak, viscous evaporite décollement. *J. Struct. Geol.* 24, 1729–1739.
- Cotton, J.T., Koyi, H.A., 2000. Modeling of thrust fronts above ductile and frictional detachments: application to structures in the Salt Range and Potwar Plateau, Pakistan. *Geol. Soc. Am. Bull.* 112, 351–363.
- Couzens-Schultz, B.A., Vendeville, B.C., Wiltshko, D.V., 2003. Duplex style and triangle zone formation: insights from physical modeling. *J. Struct. Geol.* 25 (10), 1623–1644.
- Crespo-Blanc, A., 2008. Recess drawn by the internal zone outer boundary and oblique structures in the paleomargin-derived units (Subbetic Domain, central Betics): an analogue modelling approach. *J. Struct. Geol.* 30 (1), 65–80.
- Dahlen, F.A., Suppe, J., Davis, D., 1984. Mechanics of fold-and-thrust belts and accretionary wedges: cohesive coulomb theory. *J. Geophys. Res.* 89 (B12), 10087–10101.
- Darnault, R., Callot, J.-P., Ballard, J.-F., Fraise, G., Mengus, J.-M., Ringenbach, J.-C., 2016. Control of syntectonic erosion and sedimentation on kinematic evolution of a multidecollement fold and thrust zone: analogue modeling of folding in the southern subandean of Bolivia. *J. Struct. Geol.* 89, 30–43. <https://doi.org/10.1016/j.jsg.2016.05.009>.
- Davis, D.M., Engelder, T., 1987. Thin-skinned deformation over salt. In: Lerche, I., O'Brien, J.J. (Eds.), *Dynamical Geology of Salt and Related Structures*. Academic Press, Inc., pp. 301–337.
- Davis, D., Suppe, J., Dahlen, F.A., 1983. Mechanics of fold-and-thrust belts and accretionary wedges. *J. Geophys. Res.* 88 (B12), 1153–1172.
- Davy, P., Cobbold, P.R., 1991. Experiments on shortening of a 4-layer model of the continental lithosphere. *Tectonophysics* 188 (1–2), 1–25.
- Dinarés-Turell, J., 1992. Paleomagnetisme a les Unitats Sudpirinenques Superiors. Implicacions estructurals. Tesis Doctoral. Univ. Barcelona, p. 462.
- Dixon, J.M., Summers, J.M., 1985. Recent developments in centrifuge modelling of tectonic processes: equipment, model construction techniques and rheology of model materials. *J. Struct. Geol.* 7, 83–102.
- Dixon, J.M., Spratt, D.A., 2004. Deformation at lateral ramps and tear faults—centrifuge models and examples from the Canadian Rocky Mountain Foothills. In: McClay, K.R. (Ed.), *Thrust Tectonics and Hydrocarbon Systems*, vol. 82. AAPG Mem, pp. 239–258.

- Dixon, J.M., Tirrul, R., 1991. Centrifuge modelling of fold-thrust structures in a tripartite stratigraphic succession. *J. Struct. Geol.* 13 (1), 3–20.
- Dixon, J.M., Liu, S., 1992. Centrifuge modeling of the propagation of thrust faults. In: McClay, K.R. (Ed.), *Thrust Tectonics*. Chapman & Hall, London, pp. 53–70.
- Duerto, L., McClay, K., 2009. The role of syntectonic sedimentation in the evolution of doubly vergent thrust wedges and foreland folds. *Mar. Petrol. Geol.* 26 (7), 1051–1069. <https://doi.org/10.1016/j.marpetgeo.2008.07.004>.
- Ellis, S., Schreurs, G., Panien, P., 2004. Comparisons between analogue and numerical models of thrust wedge development. *J. Struct. Geol.* 26 (9), 1659–1675.
- Fernández, O., Muñoz, J.A., Arbués, P., Falivene, O., 2012. 3-D Structure and evolution of an oblique system of relaying folds: the Ainsa basin (Spanish Pyrenees). *J. Geol. Soc. London* 169, 545–559.
- Gao, B., Flemings, P.B., Nikolinakou, M.A., Saffer, D.M., Heidari, M., 2018. Mechanics of fold-and-thrust belts based on geomechanical modeling. *J. Geophys. Res. Solid Earth* 123 (5), 4454–4474.
- Godin, L., Yakymchuk, C., Harris, L.B., 2011. Himalayan hinterland-verging superstructure folds related to foreland-directed infrastructure ductile flow: insights from centrifuge analogue modelling. *J. Struct. Geol.* 33, 329–342.
- Gracia-Puzo, F., Aubourg, C., Casas-Sainz, A., 2021. A fast way to estimate the clay fabric from shale fragments. Key example from a strained thrust footwall (Pyrenees). *J. Struct. Geol.* 152, 104443.
- Granado, P., Ferrer, O., Muñoz, J.A., Thöny, W., Strauss, P., 2017. Basin inversion in tectonic wedges: insights from analogue modelling and the Alpine-Carpathian fold-and-thrust belt. *Tectonophysics* 703–704, 50–68. <https://doi.org/10.1016/j.tecto.2017.02.022>.
- Granado, P., Ruh, J.B., Santolaria, P., Strauss, P., Muñoz, J.A., 2021. Stretching and contraction of extensional basins with pre-rift salt: a numerical modeling approach. *Front. Earth Sci.* 9, 648937. <https://doi.org/10.3389/feart.2021.648937>.
- Graveleau, F., Malavieille, J., Dominguez, S., 2012. Experimental modelling of orogenic wedges: a review. *Tectonophysics* 538–540, 1–66. <https://doi.org/10.1016/j.tecto.2012.01.027>.
- Harris, L.B., Yakymchuk, C., Godin, L., 2012. Implications of centrifuge simulations of channel flow for opening out or destruction of folds. *Tectonophysics* 526–529, 67–87.
- Hessami, K., Koyi, H.A., Talbot, C.J., Tabasi, H., Shabanian, E., 2001. Progressive unconformities within an evolving foreland fold-thrust belt, Zagros Mountains. *J. Geol. Soc.* 158, 969–981. <https://doi.org/10.1144/0016-764901-007>.
- Hill, K.C., Lucas, K., Bradey, K., 2010. Structural styles in the Papuan Fold Belt, Papua New Guinea: constraints from analogue modelling. *Geol. Soc. Lond. Spec. Pub.* 348, 33–56.
- Hindle, D., Besson, O., Burkhard, M., 2000. A model of displacement and strain for arc-shaped mountain belts applied to the Jura arc. *J. Struct. Geol.* 22 (9), 1285–1296.
- Hindle, D., Burkhard, M., 1999. Strain, displacement and rotation associated with the formation of curvature in fold belts; the example of the Jura arc. *J. Struct. Geol.* 21 (8), 1089–1101.
- Hubbert, M.K., 1937. Theory of scaled models as applied to the study of geological structures. *Bull. Geol. Soc. Am.* 48, 1459–1520.
- Huiqi, L., McClay, K., Powell, D., 1992. Physical models of thrust wedges. In: *Thrust Tectonics*. Springer, pp. 71–81.
- Izquierdo-Llavall, E., Roca, E., Xie, H., Pla, O., Muñoz, J.A., Rowan, M.G., Yuan, N., Huang, S., 2018. Influence of overlapping décollements, syntectonic sedimentation, and structural inheritance in the evolution of a contractional system: the central Kuqa fold-and-thrust belt (Tian Shan Mountains, NW China). *Tectonics* 37, 2608–2632. <https://doi.org/10.1029/2017TC004928>.
- Johns, M.K., Mosher, S., 1996. Physical models of regional fold superposition: the role of competence contrast. *J. Struct. Geol.* 18, 475–492.
- Ketcham, R., Carlson, W.D., 2001. Acquisition, optimization, and interpretation of X-ray computed tomographic imagery: applications to the geosciences. *Comput. Geosci.* 27, 381–400.
- Kohlstedt, D.L., Evans, B., Mackwell, S.J., 1995. Strength of the lithosphere: constraints imposed by laboratory experiments. *J. Geophys. Res. Solid Earth* 100 (B9), 17587–17602.
- Koyi, H., 1988. Experimental modeling of role of gravity and lateral shortening in Zagros Mountain Belt. *AAPG Bull.* 72, 1381–1394.
- Koyi, H., 1995. Mode of internal deformation in sand wedges. *J. Struct. Geol.* 17, 293–300.
- Koyi, H., 1998. The shaping of salt diapirs. *J. Struct. Geol.* 20 (4), 21–338.
- Koyi, H.A., Vendeville, B.C., 2003. The effect of décollement dip on geometry and kinematics of model accretionary wedges. *J. Struct. Geol.* 25 (9), 1445–1450.
- Lawton, T.F., Boyer, S.E., Schmitt, J.G., 1994. Influence of inherited taper on structural variability and conglomerate distribution. *Cordilleran Fold Thrust Belt Western Unit: Geology* 22, 339–342. [https://doi.org/10.1130/0091-7613\(1994\)0222.3.CO;2](https://doi.org/10.1130/0091-7613(1994)0222.3.CO;2).
- Letouzey, J., Colletta, B., Vially, R., Chermette, J.C., 1995. Evolution of salt-related structures in compressional settings. In: Jackson, M.P.A., Roberts, D.G., Snelson, S. (Eds.), *Salt Tectonics: a Global Perspective*, vol. 65. AAPG Memoir, pp. 41–60.
- Lickorish, W.H., Ford, M., Bürgisser, J., Cobbold, P.R., 2002. Arcuate thrust systems in sandbox experiments: a comparison to the external arcs of the Western Alps. *Geol. Soc. Am. Bull.* 114 (9), 1089–1107.
- Liu, H., McClay, K.R., Powell, D., 1992. Physical models of thrust wedges. In: McClay, K. R. (Ed.), *Thrust Tectonics*. Chapman & Hall, London, pp. 71–81.
- Liu, S., Dixon, J.M., 1990. Centrifuge modelling of thrust faulting. *Structural variation along strike in fold-thrust belts*. *Tectonophysics* 188, 39–62.
- Lohrmann, J., Kukowski, N., Adam, J., Oncken, O., 2003. The impact of analogue material properties on the geometry, kinematics, and dynamics of convergent sand wedges. *J. Struct. Geol.* 25 (10), 1691–1711.
- Luján, M., Storti, F., Balanyá, J.-C., Crespo-Blanc, A., Rossetti, F., 2003. Role of décollement material with different rheological properties in the structure of the Aljibe thrust imbricate (Flysch Trough, Gibraltar Arc): an analogue modelling approach. *J. Struct. Geol.* 25, 867–881.
- Luján, M., Storti, F., Rossetti, F., Crespo-Blanc, A., 2006. Extrusion vs accretion at the frictional-viscous decollement transition in experimental thrust wedges: the role of convergence velocity. *Terra. Nova* 18 (4), 241–247.
- Macedo, J., Marshak, S., 1999. Controls on the geometry of fold-thrust belt salient. *GSA Bulletin* 111, 1808–1822.
- Marques, F.O., Cobbold, P.R., 2002. Topography as a major factor in the development of arcuate thrust belts: insights from sandbox experiments. *Tectonophysics* 348, 247–268.
- Marshak, S., Wilkerson, M.S., 1992. Effect of overburden thickness on thrust-belt geometry and development. *Tectonics* 11 (3), 560–566.
- Marshak, S., 2004. Salients, recesses, arcs, oroclines, and syntaxes—A review of ideas concerning the formation of map-view curves in fold-thrust belts. In: McClay, K.R. (Ed.), *Thrust Tectonics and Hydrocarbon Systems: AAPG Memoir* 82, pp. 131–156.
- Massoli, D., Koyi, H.A., Barchi, M.R., 2006. Structural evolution of a fold and thrust belt generated by multiple décollements: analogue models and natural examples from the Northern Apennines (Italy). *J. Struct. Geol.* 28 (2), 185–199.
- Mees, F., Swennen, R., Van Geet, M., Jacobs, P., 2003. Applications of X-ray computed tomography in the geosciences. *Geol. Soc. London Spec. Pub.* 215, 1–6.
- Milazzo, F., Cavozi, C., Corti, G., Maestrelli, D., Storti, F., 2021. Centrifuge modelling of thrust systems in the brittle crust: role of frictional décollement geometry. *J. Struct. Geol.* 153, 104450. <https://doi.org/10.1016/j.jsg.2021.104450>, 2021.
- Miser, D.L., 1932. Oklahoma structural salient of the Ouachita Mountains. *Geol. Soc. Am. Bull.* 43, 1–38.
- Mitra, G., 1997. Evolution of salients in a fold-and-thrust belt: the effects of sedimentary basin geometry, strain distribution and critical taper. In: Sengupta, S. (Ed.), *Evolution of Geological Structures from Macro- to Microscales*. London. Chapman and Hall, pp. 59–90.
- Mochales, T., Casas, A.M., Pueyo, E.L., Barnolas, A., 2012. Rotational velocity for oblique structures (Boltaña anticline, Southern Pyrenees). *J. Struct. Geol.* 35, 2–16.
- Mulugeta, G., 1988. Modelling the geometry of Coulomb thrust wedges. *J. Struct. Geol.* 10 (8), 847–859.
- Mulugeta, G., Koyi, H., 1987. Three-dimensional geometry and kinematics of experimental piggyback thrusting. *Geology* 15, 1052–1056.
- Muñoz, J.A., Mencos, J., Roca, E., Carrera, N., Gratacos, O., Ferrer, O., Fernandez, O., 2018. The structure of the South-Central Pyrenean fold and thrust belt as constrained by subsurface data. *Geol. Acta: Int. Earth Sci. J.* 16 (4), 439–460. <https://doi.org/10.1344/GeologicaActa2018.16.4.7>.
- Muñoz, J.A., Beamud, E., Fernández, O., Arbués, P., Dinarès-Turell, J., Poblet, J., 2013. The Ainsa Fold and Thrust Oblique Zone of the Central Pyrenees: kinematics of a curved contractional system from paleomagnetic and structural data. *Tectonics* 32, 1142–1175.
- Munteanu, I., Willingshofer, E., Matenco, L., Sokoutis, D., Cloetingh, S., 2014. Far-field contractional polarity changes in models and nature. *Earth Planet. Sci. Lett.* 395, 101–115.
- Noble, T.E., Dixon, J.M., 2011. Structural evolution of fold-thrust structures in analog models deformed in a large geotechnical centrifuge. *J. Struct. Geol.* 33, 62–77.
- Piau, J.M., 2007. Carbopol gels: elastoviscoplastic and slippery glasses made of individual swollen sponges. Meso- and macroscopic properties, constitutive equations and scaling laws. *J. Non-Newtonian Fluid Mech.* 144 (1), 1–29.
- Pichot, T., Nalpas, T., 2009. Influence of synkinematic sedimentation in a thrust system with two décollement levels; analogue modelling. *Tectonophysics* 473, 466–475.
- Pla, O., Roca, E., Xie, H., Izquierdo-Llavall, E., Muñoz, J.A., Rowan, M.G., et al., 2019. Influence of syntectonic sedimentation and décollement rheology on the geometry and evolution of orogenic wedges: analog modeling of the Kuqa fold-and-thrust belt (NW China). *Tectonics* 38, 2727–2755. <https://doi.org/10.1029/2018TC005386>.
- Poblet, J., Muñoz, J.A., Anna, T., Serra-Kiel, J., 1998. Quantifying the kinematics of detachment folds using three-dimensional geometry: application to the Mediano anticline (Pyrenees, Spain). *Geol. Soc. Am. Bull.* 110 (1), 111–125.
- Poulin, J., 2006. De la médecine à la géologie—visualisation des modèles physiques par tomodesitométrie. M.Sc. Thesis, INRS-ETE, Québec. <http://ete.inrs.ca/pub/theses/T000478.pdf>. <http://ete.inrs.ca/pub/theses/T000478.zip>. Sept 2010.
- Ramberg, H., 1967a. Model experimentation of the effect of gravity on tectonic processes. *Geophys. J. Roy. Astron. Soc.* 14, 307–329.
- Ramberg, H., 1967b. Gravity, Deformation and the Earth's Crust as Studied by Centrifugal Models, first ed. Academic Press, London.
- Ramberg, H., 1973. Model studies of gravity-controlled tectonics by the centrifuge technique. In: de Jong, K.A., Scholten, R. (Eds.), *Gravity Tectonics*. Wiley, New York, pp. 49–66.
- Ramberg, H., 1981. Gravity, Deformation and the Earth's Crust in Theory, Experiments, and Geological Application, second ed. Academic Press, London.
- Ramsay, J.G., 1967. Folding and Fracturing of Rocks. McGraw-Hill, New York.
- Reber, J.E., Cooke, M.L., Dooley, T.P., 2020. What model material to use? A Review on rock analogs for structural geology and tectonics. *Earth Sci. Rev.* 202, 103107. <https://doi.org/10.1016/j.earscirev.2020.103107>.
- Roca, E., Sans, M., Koyi, H.A., 2006. Polyphase deformation of diapiric areas in models and in the eastern Prebetics (Spain). *AAPG (Am. Assoc. Pet. Geol.) Bull.* 90 (1), 115–136.
- Rowan, M.G., 1997. Three-dimensional geometry and evolution of a segmented detachment fold, Mississippi Fan foldbelt, Gulf of Mexico. *J. Struct. Geol.* 19, 463–480.

- Ruh, J.B., Kaus, B.J.P., Burg, J.-P., 2012. Numerical investigation of deformation mechanics in fold-and-thrust belts: influence of rheology of single and multiple décollements. *Tectonics* 31, TC3005. <https://doi.org/10.1029/2011TC003047>.
- Santolaria, P., Casas, A., Casas-Sainz, A.M., Soto, R., 2016a. Gravimetric modelling to assess salt tectonics in the western end of the south Pyrenean central unit. *J. Geol. Soc.* 174 (2), 269–288. <https://doi.org/10.1144/jgs2016-027>.
- Santolaria, P., Casas-Sainz, A.M., Soto, R., Pinto, V., Casas, A., 2014. The Naval diapir (Southern Pyrenees): geometry of a salt wall associated with thrusting at an oblique ramp. *Tectonophysics* 637, 30–44.
- Santolaria, P., Soto, R., Harris, L.B., 2016b. Influence of sedimentary density variations in décollement-related fold-and-thrust belts: insights from centrifuge analogue modelling. *Geogaceta* 60, 19–22.
- Santolaria, P., Vendeville, B.C., Graveleau, F., Soto, R., Casas-Sainz, A.M., 2015. Double evaporitic décollements: influence of pinch-out overlapping in experimental thrust wedges. *J. Struct. Geol.* 76, 35–51.
- Santolaria, P., Ayala, C., Pueyo, E.L., Rubio, F.M., Soto, R., Calvín, P., Luzón, A., Rodríguez-Pintó, A., Oliván, C., Casas-Sainz, A.M., 2020. Structural and geophysical characterization of the western termination of the South Pyrenean triangle zone. *Tectonics* 39, e2019TC005891. <https://doi.org/10.1029/2019TC005891>.
- Scharer, K.M., Burbank, D.W., Chen, J., Weldon, R.J., Rubin, C., Zhao, R., Shen, J., 2004. Detachment folding in the Southwestern Tian Shan-Tarim foreland, China: shortening estimates and rates. *J. Struct. Geol.* 26, 2119–2137.
- Schellart, W.P., 2000. Shear test results for cohesion and friction coefficients for different granular materials: scaling implications for their usage in analogue modeling. *Tectonophysics* 324, 1–16. [https://doi.org/10.1016/S0040-1951\(00\)00111-6](https://doi.org/10.1016/S0040-1951(00)00111-6).
- Schreurs, G., Hänni, R., Vock, P., 2001. 4D analysis of analog models: experiments on transfer zones in fold and thrust belts. In: Koyi, H.A., Mancktelow, N.S. (Eds.), *Tectonic Modeling: A Volume in Honor of Hans Ramberg*. Geological Society of America Memoirs, Boulder, Colorado, pp. 179–190.
- Schreurs, G., Hänni, R., Panien, M., Vock, P., 2003. Analysis of analogue models by helical X-ray computed tomography. *Geol. Soc. London Special Pub.* 215 (1), 213–223. <https://doi.org/10.1144/gsl.sp.2003.215.01.2>.
- Scott Wilkerson, M., Smaltz, S.M., Bowman, D.R., Fischer, M.P., Higuera-Díaz, I.C., 2007. *J. Struct. Geol.* 29, 73–85.
- Sempere, T., 1995. Phanerozoic evolution of Bolivia and adjacent regions. In: Tankard, A.J., Soruco, R.S., Welsink, H.J. (Eds.), *Petroleum Basins of South America*, vol. 62. American Association of Petroleum Geologists Memoir, pp. 207–230.
- Shafiei, M., Balhoff, M., Hayman, N.W., 2018. Chemical and microstructural controls on viscoplasticity in Carbopol hydrogel. *Polymer* 139, 44–51.
- Smit, J., Burg, J.-P., Dolati, A., Sokoutis, D., 2010. Effects of mass waste events on thrust wedges: analogue experiments and application to the Makran accretionary wedge. *Tectonics* 29 (TC3003).
- Smit, J.H.W., Brun, J.P., Soukoutis, D., 2003. Deformation of brittle–ductile thrust wedges in experiments and nature. *J. Geophys. Res.* 108 (B10), 2480. <https://doi.org/10.1029/2002JB002190>.
- Snidero, M., Carrera, N., Mencos, J., Butillé, M., Granado, P., Tavani, S., López-Mir, B., Sábato, F., Muñoz, J.A., 2020. Diapir kinematics in a multi-layer salt system from the eastern Persian Gulf. *Mar. Petrol. Geol.* 117, 104402. <https://doi.org/10.1016/j.marpetgeo.2020.104402>.
- Soto, R., Storti, F., Casas, A.M., Faccenna, C., 2003. Influence of along-strike pre-orogenic sedimentary tapering on the internal architecture of experimental thrust wedges. *Geol. Mag.* 140, 253–264.
- Soto, R., Casas-Sainz, A.M., Pueyo, E.L., 2006. Along-strike variation of orogenic wedges associated with vertical axis rotations. *J. Geophys. Res.* 111, B10402. <https://doi.org/10.1029/2005JB004201>.
- Soto, R., Casas, A.M., Storti, F., Faccenna, C., 2002. Role of lateral thickness variations on the development of oblique structures at the western end of the South Pyrenean Central Unit. *Tectonophysics* 350, 215–235.
- Soto, R., Vendeville, B.C., Graveleau, F., 2020. Interaction between perpendicularly-trending thrust wedges and its impact on foreland deformation: insights from analogue modelling. *Tectonophysics*, 228462. <https://doi.org/10.1016/j.tecto.2020.228462>.
- Stockmal, G.S., Beaumont, C., Nguyen, M., Lee, B., 2007. Mechanics of thin-skinned fold-and-thrust belts: insights from numerical models. *Geol. Soc. Am. Spec. Pap.* 433, 63–98.
- Storti, F., Salvini, F., McClay, K., 2000. Synchronous and velocity-partitioned thrusting and thrust polarity reversal in experimentally produced, doubly-vergent thrust wedges: implications for natural orogens. *Tectonics* 19 (2), 378–396.
- Storti, F., Soto Marín, R., Rossetti, F., Casas-Sainz, A.M., 2007. Evolution of experimental thrust wedges accreted from along-strike tapered, silicone-floored multilayers. *J. Geol. Soc. London* 164, 73–85.
- Storti, F., Soto-Marin, R., Faccenna, C., Casas-Sainz, A.C., 2001. Role of the backstop-to-cover thickness ratio on vergence partitioning in experimental thrust wedges. *Terra Nova* 13 (6), 413–417.
- Sussman, A.J., Butler, R.F., Dinarès-Turell, J., Vergés, J., 2004. Vertical-axis rotation of a foreland fold and implications for orogenic curvature: an example from the Southern Pyrenees, Spain. *Earth Planet Sci. Lett.* 218, 435–449.
- ten Grotenhuis, S.M., Piazolo, S., Pakula, T., Passchier, C.W., Bons, P.D., 2002. Are polymers suitable rock analogs? *Tectonophysics* 350, 35–47.
- Turrini, C., Ravaglia, A.S., Perotti, C.R., 2001. Compressional structures in a multilayered mechanical stratigraphy: insights from sandbox modelling with three-dimensional variations in basal geometry and friction. In: Koyi, H.A., Mancktelow, N.S. (Eds.), *Tectonic Modeling: A Volume in Honor of Hans Ramberg*. Geological Society of America Memoirs, Boulder, Colorado, pp. 153–178.
- Van Keken E., P., Spiers J., C., van den Berg P., A., Muylert J., E., 1993. The effective viscosity of rocksalt: implementation of steady-state creep laws in numerical models of salt diapirism. *Tectonophysics* 225, 457–476. [https://doi.org/10.1016/0040-1951\(93\)90310-G](https://doi.org/10.1016/0040-1951(93)90310-G).
- Vidal-Royo, O., Koyi, H.A., Munoz, J.A., 2009. Formation of orogen-perpendicular thrusts due to mechanical contrasts in the basal décollement in the Central External Sierras (Southern Pyrenees, Spain). *J. Struct. Geol.* 31 (5), 523–539.
- Waffle, L., Godin, L., Harris, L.B., Kontopoulou, M., 2016. Rheological and physical characteristics of crustal-scaled materials for centrifuge analogue modelling. *J. Struct. Geol.* 86, 181–199. <https://doi.org/10.1016/j.jsg.2016.02.014>.
- Weijermars, R., Jackson, M.P.A., Vendeville, B.C., 1993. Rheological and tectonic modeling of salt provinces. *Tectonophysics* 217, 143–174.
- Weil, A.B., Van der Voo, R., van der Pluijm, B.A., Parés, J.M., 2000. Unraveling the timing and geometric characteristics of the Cantabria-Asturias Arc (northern Spain) through paleomagnetic analysis. *J. Struct. Geol.* 22, 735–756. [https://doi.org/10.1016/S0191-8141\(99\)00188-1](https://doi.org/10.1016/S0191-8141(99)00188-1).
- Weil B., A., Sussman J., A., 2004. Classifying curved orogens based on timing relationships between structural development and vertical-axis rotations. *Orogenic Curvature: Integrating Paleomagnetic and Structural Analyses*, 383. Geological Society of America Special Paper, pp. 1–15.
- Weil, A.B., Van der Voo, R., van der Pluijm, B., 2001. New paleomagnetic data from the southern Cantabria-Asturias Arc, northern Spain: implications for true oroclinal rotation and the final amalgamation of Pangea. *Geology* 29, 991–994. [https://doi.org/10.1130/0091-7613\(2001\)0292.0.CO;2](https://doi.org/10.1130/0091-7613(2001)0292.0.CO;2).
- Weil, A.B., Yonkee, W.A., 2012. Layer-parallel shortening across the Sevier fold-thrust belt and Laramide foreland of Wyoming: spatial and temporal evolution of a complex geodynamic system. *Earth Planet Sci. Lett.* 357, 405–420.
- Yakymchuk, D., Harris, L.B., Godin, L., 2012. Centrifuge modelling of deformation of a multi-layered sequence over a ductile substrate: 1. Style and 4D geometry of active cover folds during layer-parallel shortening. *Int. J. Earth Sci.* 101, 463–482.